3-10-2022

Lakshadweep High Propagation and Impacts on the Somali Current and Eddies During the Southwest Monsoon

Paul A. Ernst

Bulusu Subrahmanyam
University of South Carolina - Columbia, sbulusu@geol.sc.edu

Corinne B. Trott

Publication Info

Published in *JGR Oceans*, Volume 127, Issue 3, 2022.

JGR Oceans

RESEARCH ARTICLE
10.1029/2021JC018089

Lakshadweep High Propagation and Impacts on the Somali Current and Eddies During the Southwest Monsoon

Paul A. Ernst[1], **Bulusu Subrahmanyam**[1], **and Corinne B. Trott**[2]

[1]School of the Earth, Ocean, and Environment, University of South Carolina, Columbia, SC, USA, [2]Naval Research Laboratory, Stennis Space Center, MS, USA

Key Points:

- We track the Lakshadweep High (LH) and analyze its complete life cycle for the first time over a 27-year period
- The LH propagates in three modes based on its decoherence location, reaching the Somali Current (SC) region in a majority of years
- Longer LH propagation modes reduce Great Whirl and SC region eddy kinetic energy during the summer monsoon

Supporting Information:

Supporting Information may be found in the online version of this article.

Correspondence to:

P. A. Ernst,
pernst@seoe.sc.edu

Citation:

Ernst, P. A., Subrahmanyam, B., & Trott, C. B. (2022). Lakshadweep High propagation and impacts on the Somali Current and eddies during the southwest monsoon. *Journal of Geophysical Research: Oceans*, *127*, e2021JC018089. https://doi.org/10.1029/2021JC018089

Received 30 SEP 2021
Accepted 6 MAR 2022

Author Contributions:

Conceptualization: Bulusu Subrahmanyam
Data curation: Paul A. Ernst, Bulusu Subrahmanyam
Formal analysis: Paul A. Ernst, Bulusu Subrahmanyam, Corinne B. Trott
Funding acquisition: Bulusu Subrahmanyam
Investigation: Paul A. Ernst, Bulusu Subrahmanyam, Corinne B. Trott
Methodology: Paul A. Ernst, Corinne B. Trott
Project Administration: Bulusu Subrahmanyam
Resources: Bulusu Subrahmanyam

Abstract Climatological eddies in the Arabian Sea (AS), including the Lakshadweep High (LH) and the Great Whirl (GW), play major roles in the regional fluxes of upper ocean properties. For the first time, we apply an eddy tracking algorithm to the LH using altimetric sea surface height observations from 1993 through 2019. We additionally analyze the LH's water mass composition throughout its life cycle using the 1/12° Global eddy resolving physical ocean and sea ice reanalysis (GLORYS12). We observe that the second annual downwelling coastal Kelvin wave's (CKW) arrival during the winter monsoon is primarily responsible for generating the LH. In March, Rossby waves propagate along 8°N at the same speed of that of the LH. In 17 of 27 years, the LH maintains coherence across the AS. The LH sustains a shallow lens of lower salinity Bay of Bengal water up to 68°E in these years. In the remaining 10 years, the LH dissipates between 60°E and 70°E or fails to propagate beyond the southwest Indian coast. We attribute the differences between propagation types to fluctuations in the CKW strength, differences in wind stress between the southern tip of India and Sri Lanka, and the variable distribution of wind stress curl around the LH. We also find that longer propagating LH types negatively correlate with the eddy kinetic energy of the Somali Current region during the summer monsoon. We conclude that, upon its arrival in late July, the LH either merges with or replaces the GW, disrupting the cyclone that normally orbits the GW.

Plain Language Summary Mesoscale ocean vortices known as eddies exist on the scale of 10–100 km and play a large role in moving water around the oceans. Eddies are important to understand when researching how properties like temperature are globally distributed. Some specific eddies in the Arabian Sea (AS), like the Lakshadweep High (LH), are seasonally consistent in where and when they form. In this study, we examine the LH in detail, describing how it develops, grows, propagates, and dissipates as well as the possible mechanisms for each of these steps. We find that the LH has three distinct life cycles based on where it dissipates. We attribute the differences in life cycles to the variable extent of certain planetary waves as well as the amount and type of wind applied to the surface ocean near the Indian coast. We also note that the type of LH life cycle correlates with changes in the characteristics of the Somali Current (SC) on the other side of the AS. We investigate this connection and conclude that the arrival of the LH in the SC region may interrupt the development of a large eddy that would otherwise normally form around early August each year.

1. Introduction

Oceanic mesoscale eddies are circulation features that contribute significantly to fluxes across the air-sea interface and transport seawater properties throughout the global oceans (Ma et al., 2016; Zhang et al., 2014). Previous studies have indicated the relative importance of eddy dynamics to broader circulation patterns and the distribution of physical parameters, such as temperature and salinity, in the Arabian Sea (AS) (Fischer et al., 2002; Trott, Subrahmanyam, Chaigneau, Delcroix, 2018; Trott, Subrahmanyam, Chaigneau, Roman-Stork, 2019; Zhan et al., 2020). The AS is additionally characterized by seasonal variability due to the reversal of winds associated with the northeastern monsoon in the boreal winter and the southwestern monsoon in the boreal summer (Beal et al., 2013; Schott & McCreary, 2001). This circulation reversal results in the recurring development of several distinct, quasi-permanent eddies that form and dissipate within the AS each year (Akuetevi et al., 2016). These include the Lakshadweep (sometimes named Laccadive) High (LH) and the Great Whirl (GW), among others (Figure 1). Each of these features has been subjected to observational and numerical model investigations that have shed light on their respective formation mechanisms and interannual variability (Beal & Donohue, 2013; Bruce, 1983; Bruce et al., 1994, 1998; Vic et al., 2014). However, while the spatial variability of the GW has been extensively described both manually (Beal et al., 2013) and algorithmically (Melzer et al., 2019; Wang

Software: Paul A. Ernst, Corinne B. Trott
Supervision: Bulusu Subrahmanyam
Visualization: Paul A. Ernst, Bulusu Subrahmanyam, Corinne B. Trott
Writing – original draft: Paul A. Ernst
Writing – review & editing: Paul A. Ernst, Bulusu Subrahmanyam, Corinne B. Trott

et al., 2019), the LH's complete life cycle has yet to be rigorously classified and tracked in the context of an eddy tracking algorithm, leaving questions regarding the interannual variability of the LH, including its propagation mechanism, its characteristics while propagating, and its ultimate fate in the AS basin.

The LH is an anticyclonic eddy (AE) that forms during the northeast monsoon off the west coast of India and to the east of the Lakshadweep islands (Figure 1a). It was first identified by Bruce et al. (1994), and later more specifically characterized in terms of linear planetary wave dynamics by Shankar and Shetye (1997). The formation mechanism of the LH put forward by these initial studies and later supported by a numerical study by Kurian and Vinayachandran (2007) is that the LH is a result of the second annual downwelling coastal Kelvin wave (CKW) arriving from the Bay of Bengal (BoB) in the late boreal fall and early winter (Rao et al., 2010), traveling northward along the western coast of India and radiating westward-propagating Rossby waves. It is worth noting that this same CKW is associated with the transport of low-salinity BoB waters around the tip of Sri Lanka and into the southeastern Arabian Sea (Shenoi et al., 2005). Therefore, eddies produced along these CKWs are more likely to have a fresher core water mass than the surrounding AS waters. After forming in late December or early January, the LH detaches from the coast and propagates westward across the AS, most likely as a part of a Rossby wave, before appearing to become indistinct in mid basin by March (Bruce et al., 1998; Prasad & Ikeda, 2001). Although the Lakshadweep Low (the LH's summertime component) has been recently observationally and dynamically described (Zachariah et al., 2019), no study has specifically examined the LH's interannual variability, its observed life cycle over recent years, or its impacts on the rest of the AS circulation, such as the SC.

As the LH's dynamics can be largely explained in terms of planetary waves, it is important to understand the role Rossby waves play in the AS basin. The propagation of Rossby waves westward across the AS has been well documented (Brandt et al., 2002; Heffner et al., 2008; Subrahmanyam et al., 2001, 2009; Tozuka et al., 2014). The Rossby waves radiated by the second annual downwelling CKW in particular have been demonstrated in a modeling study by Vic et al. (2014) to significantly alter the characteristics of the GW. In their "NO-RW" experiment, they modeled a situation wherein the Rossby waves from the west coast of India are blocked from propagating across the AS basin. They found that the development of the GW was delayed by nearly 2 months as compared to the same model run with the Rossby waves allowed to propagate. Furthermore, they observe that the location of the GW is shifted 250 km to the southeast. This study provides compelling evidence toward the hypothesis of Beal and Donohue (2013) that the arrival of first- and second-baroclinic mode Rossby waves kickstart the formation of the GW and help determine its final location in the SC. Due in part to the size of the GW and its cold filament, as well as the intensity of the SC, there is a stable correlation between the sea surface temperature (SST) of the western AS, the strength of the atmospheric Findlater Jet that overlies the SC, and the quantity of summer monsoon precipitation over India (Findlater, 1969; Izumo et al., 2008; Murtugudde & Busalacchi, 1999; Seo, 2017; Shukla, 1975; Vecci et al., 2004; Wang et al., 2019). This sequence of correlations between the development of the GW and the SC and the summer monsoon as a whole highlights the importance of understanding the factors that influence the GW and the SC, as well as documenting the effects and variability of Rossby waves in the region.

Advances in satellite altimetry have yielded global observations with resolutions sufficiently high to track mesoscale eddies. Many authors have since developed automated eddy-tracking algorithms based on various physical properties, such as sea surface height anomaly (SSHA, used interchangeably sea level anomaly, or SLA), absolute dynamic topography (ADT), the Okubo-Weiss parameter, and others (Chaigneau et al., 2008; Chelton et al., 2011; Franz et al., 2018; Le Vu et al., 2018; Williams et al., 2011). Previous studies have since improved the accuracy of these algorithms (Pegliasco et al., 2015; Trott, Subrahmanyam, Chaigneau, Delcroix, 2018) and have used them to track merging eddies (Cui et al., 2019; de Marez et al., 2020), as well as the life cycles of specific large eddies, such as the GW (Melzer et al., 2019). Thanks to advances in the number of floats and drifters available through initiatives such as Argo and the Global Drifter Program (GDP) as well as the accuracy of ocean circulation model and reanalysis products, these eddy tracking algorithms can even be used to provide estimates of the 3D structure of eddies over time, including in the AS (de Marez et al., 2019; Greaser et al., 2020; L'Hégaret et al., 2016; Trott, Subrahmanyam, Chaigneau, Delcroix, 2018).

In this study, we apply an automatic eddy tracking algorithm to 27 years of ADT satellite data from 1993 to 2019 in the AS. In doing so, we analyze the life cycles, trajectories, and properties of the LH in order to better understand it and the ways it may influence the interannual variability of the monsoon phenomenon. We provide the first 3D analysis of the LH and shed light on its subsurface profiles, interannual variability, and impacts on the

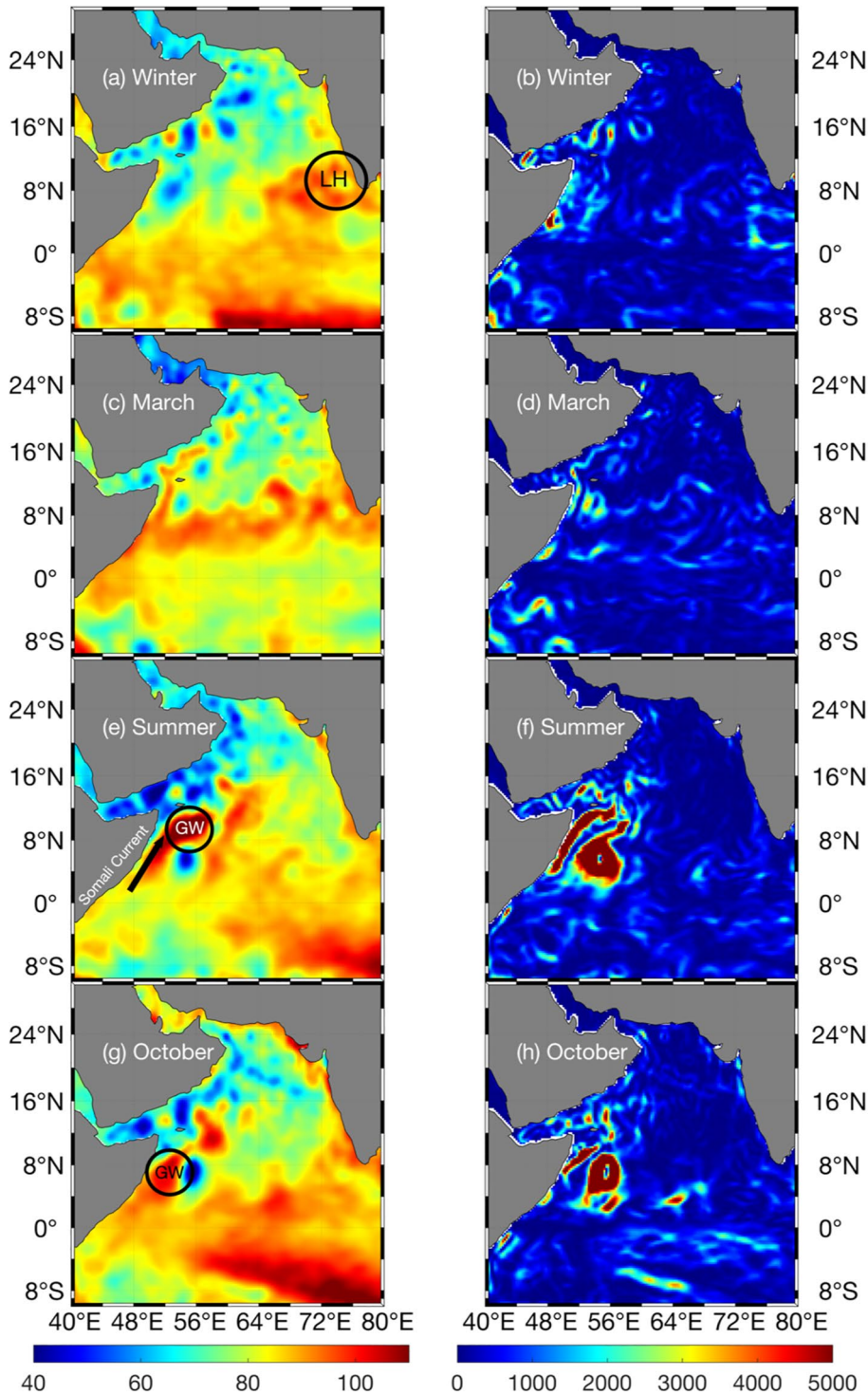

Figure 1. Mean absolute dynamic topography (ADT) (cm) during winter (mean of November, December, January, and February) (a), March (c), summer (mean of May, June, July, August, and September) (e), and October (g), averaged from 1993 to 2019. (b, d, f, and h),: Same as (a, c, e, and g) but for eddy kinetic energy (EKE) ($cm^2\ s^{-2}$). The locations of the LH, the GW, and the Somali Current (SC) are annotated.

rest of the AS, including the SC region and the GW within. The rest of the paper will be organized as follows. Section 2 describes our data and methodology. Section 3 presents our results, while Section 4 summarizes and concludes our findings.

2. Data and Methods

2.1. Data Used

ADT, SLA, and derived surface geostrophic currents used in this work are provided by the Copernicus Marine and Environmental Monitoring Service (CMEMS). This product is currently available daily from 1993 through June 2020 at a 0.25° global grid spacing resolution and is an optimal interpolation of altimetry satellites, merging observations from TOPEX/POSEIDON, HY-2A, JASON-1, JASON-2, JASON-3, ENVISAT, Saral/AltiKa, ERS1/2, Sentinel-3A, and GFO. The data set is computed with respect to a 20-year mean (Ducet et al., 2000; Le Traon et al., 1998) and has been recently used to track eddies in the AS (Trott, Subrahmanyam, Chaigneau, Delcroix, 2018). This data set is available online from CMEMS at https://marine.copernicus.eu.

To obtain wind stress and compute wind stress curl (WSC), we use the U.S. National Oceanic and Atmospheric Administration (NOAA) Blended Winds Data set, a 0.25° global grid resolution data set daily from 1987 to 2021. The winds from this data set are combined from all available satellite wind measurements, scaling from a single satellite in 1987 to more than 5 after 2000, including SSMI F13, SSMI F14, SSMI F15, TMI, QuikSCAT, and AMSR-E. This product is available from NOAA at https://www.ncei.noaa.gov/products/blended-sea-winds and has similarly been used in studies of the Indian Ocean and its monsoons (Liu et al., 2015).

We use ocean drifter surface location and current velocity data from the NOAA Global Drifter Program (GDP) to illustrate and validate the trajectories of our tracked eddies. These data are available at 6-hourly interval basis from 1979 through 2020, and provides an in situ method for measuring surface currents around and within eddies in the AS (de Marez et al., 2019). This product is available at http://osmc.noaa.gov/.

To obtain estimates for subsurface data, including temperature, salinity, and currents, we use the CMEMS 1/12° Global eddy resolving physical ocean and sea ice reanalysis (GLORYS) 12v1, the next generation product with respect to the GLORYS2v4 data set (Lellouche et al., 2018). This is a 1/12° spatial resolution global data set available daily for the altimetry era (1993–2021). It assimilates observational data from satellite and in situ data sets while its model component is based off of the Nucleus for European Modeling of the Ocean (NEMO) model 3.1 driven at the surface by European Center for Medium-Range Weather Forecasts (ECMWF) ERA-interim analysis. It additionally incorporates climatological runoff from Dai et al. (2009). This data set was chosen due to its high spatiotemporal resolution and focus on accurate comparisons to observational CMEMS data sets of SSH, freshwater content, and EKE. Additionally, Verezemskaya et al. (2021) found GLORYS12v1 was the most accurate reanalysis data set of the data sets they studied when used to study the variability of various ocean characteristics along a section of latitude in the ocean, an ultimately similar task to our study. GLORYS12v1 is available online at https://marine.copernicus.eu.

2.2. Methodology

2.2.1. Eddy Tracking

In order to sufficiently describe the LH and its impacts on the GW and the SC, we must first be able to identify it discretely and track it over time and space. In order to classify eddies and map their trajectories, we apply the closed-contour eddy tracking algorithm developed by Chaigneu et al. (2008), upgraded by Pegliasco et al. (2015) and used throughout the Indian Ocean by Roman-Stork et al. (2020), Trott, Subrahmanyam, Chaigneau, and Delcroix (2018), Trott, Subrahmanyam, Chaigneau, and Roman-Stork (2019), and Greaser et al. (2020). As compared to other eddy methods, this method is threshold-free, detects a fewer number of false eddies, and allows for a more exact eddy shape. A complete explanation of the algorithm as applied here, including the cost function used for tracking eddy centers, can be found in Trott, Subrahmanyam, Chaigneau, and Delcroix, (2018).

2.2.2. LH & GW Classification

The first step in tracking the impacts of the LH is correctly classifying the characteristic LH. While a previous study by Bruce et al. (1998) has correctly identified that the LH region generates multiple eddies, there is typically

a single eddy that consistently dominates the circulation of the region after late December. It is this eddy that we examine here and refer to as "LH." To this end, after we applied the eddy tracking algorithm to the altimetry data set, we filtered for all eddy trajectories that passed within the zone between 5°N–15°N and 71°E–80°E. We then additionally filtered for eddies that originated between the beginning of November and the end of January of each year. This spatiotemporal area was chosen based upon an evaluation of the preceding research (Bruce et al., 1998; Shankar & Shetye, 1997), the internationally recognized boundaries of the Laccadive Sea, and our own observations made in the ADT of the region over our 27-year timespan (Figure 1a). Once all eddies outside of this area were excluded, the eddies that passed inside the area were ranked from greatest to least in terms of their lifespan and maximum radius. The minimums of the sums of these rankings (e.g., the longest lived trajectory, ranked first, with the second highest maximum radius, ranked second, is equal to a sum of $1 + 2 = 3$) were classified as major eddies within the region. This radius-ranking procedure is similar to the criteria used by Trott, Subrahmanyam, Chaigneau, and Delcroix (2018) to identify the GW, although we add the lifetime ranking to reduce the weight given to short-lived, large-radius outliers. This allowed us to narrow down the 108,883 individual trajectories down to a ranked list of the largest, longest lived eddies each year.

After this initial automatic classification, a manual examination was conducted on ADT maps of the region over all years, and the automatic trajectories were checked against the LH region. In 18 of the 27 years, the primary candidate identified by the automatic classification was correct in identifying the LH. However, the remaining 9 years, our initial algorithm falsely identified a signature corresponding to a characteristic eddy of the Southern Arabian High (SAH) as defined by Prasad and Ikeda (2001). This signal was initially difficult to differentiate from the LH automatically due to their near-identical origin points off the southern tip of India and similar eventual large size. However, our manual reevaluation allowed a correction of these trajectories, as the SAH eddies propagate along 6°N beginning in December and January, while the LH eddies propagate along 8°N beginning in February and March. Adjusting the initial automatic selection criteria for eddies that remain in close proximity to 8°N for most of their lives results in a correct automatic identification of the LH 95% of the time. The outlier in this case is the year 2000, where manual examination reveals an LH that proceeds to join the SAH along 6°N.

We conducted the same ranking analysis followed by manual confirmation in order to identify the GW. In this case, the ranking algorithm's initial eddy selection was correct in all years as confirmed by previous studies of the GW (Beal & Donohue, 2013; Melzer et al., 2019). It is worth noting that in 10 of the 27 years studied, the SAH was directly identified as the GW with the same tracking number, indicating a persistent closed contour of ADT through the entire period. In 15 of the remaining years, the tracking number assigned to the GW was one of the SAH's direct descendants (i.e., an eddy that split off from the SAH) as identified by our tracking algorithm. However, an analysis of the linkage between the SAH and the GW is outside of the scope of the present study.

2.2.3. Vertical Velocity

As in Greaser et al. (2020), we calculate the vertical velocity (w) using the zonal (u) and meridional (v) components of ocean currents from GLORYS12v1 by integrating the continuity equation:

$$\frac{\partial w}{\partial z} = -\left(\frac{\partial u}{\partial z} + \frac{\partial v}{\partial z}\right) \tag{1}$$

2.2.4. Spiciness

The definition of spiciness used in our eddy analysis is the same one described by McDougall and Krzysik (2015) and implemented in the TEOS-10 Gibbs SeaWater (GSW) Oceanographic Toolbox. We use spiciness referenced to the surface as demonstrated in the AS by Echols and Riser (2020).

2.2.5. Wind Work

Our definition and application of wind work to our analysis is defined in the same way as in Zhang et al. (2017):

$$WW = \overline{\tau_w \cdot v_0'}, \tag{2}$$

where τ_w denotes the wind stress and v_0 is the surface horizontal velocity. As in Zhang et al. (2017), the overbar reflects a time mean, while the prime denotes anomalies from that time mean.

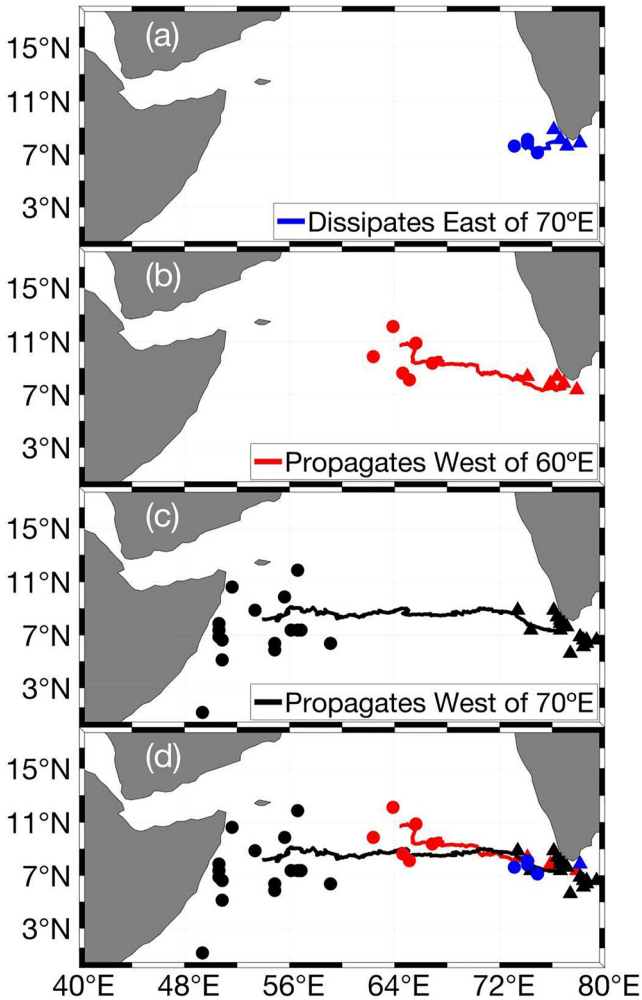

Figure 2. The original (filled triangles) and final (filled circles) locations tracked for each LH, 1993–2019. The lines indicate an average of all trajectories of a given type based off of the average origin point through the final recorded location at the mean lifetime of the propagation type. Blue objects and lines in (a) indicate trajectories that do not pass 70°E. Red objects and lines in (b) indicate trajectories that are recorded passing 70°E, but dissipating before passing 60°E. Black objects and lines in (c) indicate trajectories that are recorded passing 60°E, (d) displays all trajectory clusters on the same panel for comparison.

2.2.6. Radon Transform

We use a two-dimensional Radon Transform (RT) to calculate Rossby wave speed in the AS. The use of the RT in regard to Rossby waves is the same as Deans (2007) and Challenor et al. (2001). We begin with a longitude-time (L/T) plot, in our case, a Hovmöller diagram of SLA. Then, the RT projects the diagram onto a line at an angle, θ, to the x-axis. The values along this line are taken with the angle varied from 0° to 180°. The standard deviation of the values on this line will be at its maximum when the line is perpendicular to the propagation direction of the Rossby wave and, as such, the speed of the wave can be obtained by taking the tangent of θ at the angle of maximum standard deviation:

$$c_{RW} = \tan(\theta) \cdot \cos(\varphi) \quad (3)$$

where φ is the degree of latitude of the L/T plot. In this study, we plot both the cumulative intensity image directly output by the RT as well as the standard deviation of the SLA in the cumulative intensity image.

3. Results

3.1. Overview of LH Trajectory Types by Year

Upon identifying the trajectories corresponding to the LHs, we proceed to map out their origin points, the points at which their trajectories terminate and the average trajectories of the LH propagation (Figure 2).

The end behavior of the LH is classifiable into three distinct groups depending upon the termination point of the eddy track (the point at which the closed contour breaks and the eddy ceases being a closed, coherent whirl). The most numerous, occurring in 17 out of the 27 years, is the propagation type in which the LH is able to remain coherent past 60°E, most often reaching the outermost contour of the GW before dissipating. For the rest of this study, we refer to this type of propagation as "full" and the years in which this type occurs as "full years." The second most common, occurring in 6 of the remaining years, is a type in which the LH begins propagating across the AS basin but loses coherence between 60°E and 70°E, roughly the halfway point between Somalia in the west and India in the east. It is for this reason that we will refer to this type of propagation and its years as "half" and "half years", respectively. Finally, in the remaining 4 years, the LH may move slightly off the west coast of India, but never propagates west of the Lakshadweep islands. Due to its lack of movement away from its origin, we deem this type the "local" type and its years "local years." The total list of year wise classification, along with relevant climatic phenomena, such as the El Niño Southern Oscillation (ENSO) and the Indian Ocean Dipole (IOD) is in Table 1.

It is worth noting in Table 1 that, as the LH forms late in the previous year, the formation circumstances of each year's LH are owed primarily to the previous year. In Table 1, strong (weak) monsoons are defined by total monsoon rainfall that is 10% above (below) the long term mean (Subrahmanyam et al., 2020). We note that both strong monsoons are half years, while every local year occurs either on or after an El Niño event. However, other El Niño years precede full years (e.g., 2015). Based on this distribution, we conclude that the full propagation type represents a relatively normal state for the LH and that specific changes to the generation and development of the LH are necessary to explain the difference between these typical years and the atypical half and local years. We further discuss the connection between El Niño, IOD, and half/local years in Section 3.2.

We display years that best illustrate the notable features of LH's type of propagation. As the development and propagation of LH occurs on slightly different timescales and in slightly different locations each year, choosing

Table 1
Yearwise Southwest Monsoon Strength (Second Column), Occurrences of El Niño Southern Oscillation (ENSO) Phase (Third Column), IOD Phase (Fourth Column), and LH Type of Propagation (Fifth Column) From 1993 to 2019

Year	Monsoon	ENSO	IOD	LH
1993				Full
1994	Strong	El Niño	Positive	Half
1995		La Niña		Full
1996			Negative	Full
1997		El Niño	Positive	Local
1998		La Niña	Negative	Local
1999		La Niña		Half
2000		La Niña		Full
2001				Full
2002	Weak	El Niño		Full
2003				Half
2004	Weak	El Niño		Local
2005		La Niña		Full
2006		El Niño	Positive	Full
2007		La Niña		Full
2008		La Niña		Full
2009	Weak	El Niño		Full
2010		La Niña	Negative	Local
2011		La Niña		Half
2012			Positive	Full
2013				Half
2014	Weak	El Niño	Negative	Full
2015	Weak	El Niño	Positive	Full
2016	Weak	La Niña	Negative	Full
2017				Full
2018		La Niña		Full
2019	Strong		Positive	Half

Note. Example years are highlighted. Table entries without an explicit designation are neutral in their respective indices. Columns 2, 3, and 4 are adapted from Roman-Stork et al. (2020)

example years allows us to highlight common features that geographic composites may disperse due to the averaging process over both time and space. We choose 2006 for full propagation, 1994 for half propagation, and 1998 for local propagation. These years in particular are chosen because these years' LHs develop and propagate on similar timescales (i.e., Figure 3) and demonstrate most of the unique features of their respective propagation types. As a result, their development can be compared to each other at the same time in their respective years. Additionally, the 1994 LH is the LH analyzed by Bruce et al. (1998), allowing us to highlight differences between studies.

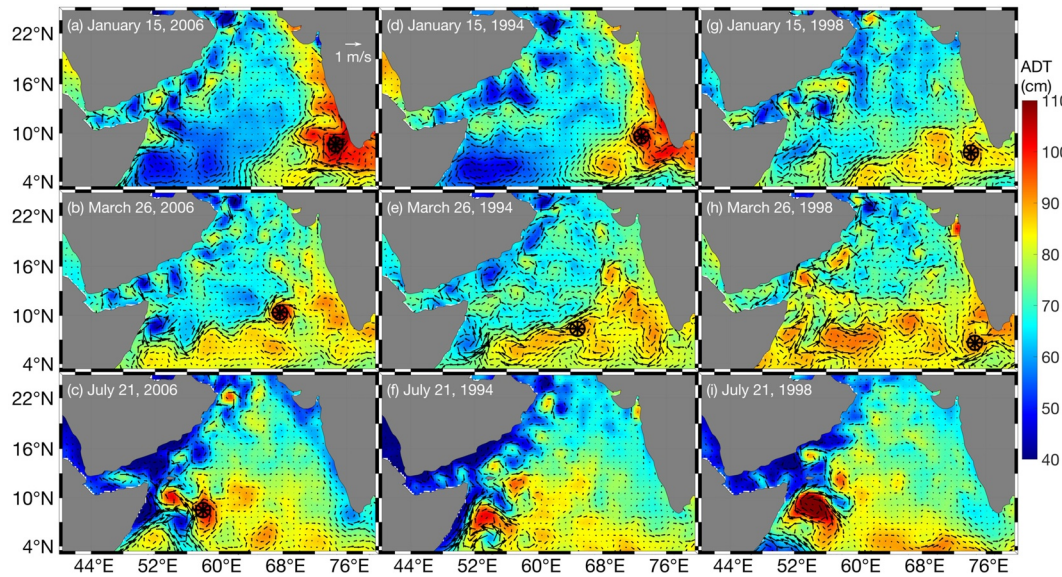

Figure 3. Absolute dynamic topography (ADT) (cm) of the Arabian Sea (AS) in 2006, 1994, and 1998. Arrows depict geostrophic current vectors (m s^{-1}) from altimetry data. Black pinwheels mark locations of the tracked Lakshadweep High (LH) at the given times. (a–c) 15 January, 16 March, and 21 July 2006. (d–f) Same as (a–c) but for 1994 (m–r) Same as (a–c) but for 1998.

We observe that the high encompassing the LH in the winter monsoon is greater in extent in 2006 (470,000 km^2, Figure 3a) than in 1994 (384,000 km^2, Figure 3d), and that the same region in 1994 is larger than in 1998 (110,000 km^2, Figure 3g). This high is determined via a 10-cm SLA threshold; this was chosen to align with Rao et al. (2010), where the 10 cm threshold is used to define a "strong" equatorial Kelvin wave in the Indian Ocean. Here, we use the threshold in much the same way, using it to define the extent of strongest CKW influence, both here and in Section 3.2. Upon examination of the GW in the summer monsoon, we find that the 2006 LH is directly influencing the GW in July (Figure 3c) while the 1998 GW is much larger and more coherent at the same time of the year (Figure 3i). As noted by Beal and Donohue (2013), the 1998 GW remains the largest GW on record.

To further examine the LH trajectories of these years, we collocate each LH with drifters from the GDP (Figure 4). We find that the 2006 LH influenced two drifters in its early lifetime while trapping four more much later in its life. We attribute this latter phenomenon to the fact that the LH enters the SC region as the GW shifts toward the island of Socotra (Figure 3c), growing and remaining in place in the SC for the rest of the calendar year. As a result, the 2006 LH spends the last months of its life largely stationary and thereby with more capacity for the recirculation of an individual drifter (Figure 4a). This stationary aspect is the same for the 1998 LH, as it captures a single drifter, which circulates about the LH for 50 days (Figure 4c). The 1994 LH did not capture any drifters, likely due to the paucity of drifters in the AS as compared to later years, as well as the fact that it does not remain stationary for a long period of time, as the 2006 and 1998 LHs do (Figure 4b).

Here, we compute the error between the geostrophic currents derived from altimetric observations and the surface currents measured by drifters. Across all LH trajectories, this error averages 43%, while the error for the specific trajectories in Figure 4 is 57%. This average error is plausible for eddies within the AS (de Marez et al., 2019), as the expected range of errors varies from negligible error at the edges of eddies to 500% at the center. It is worth noting that the average error present in the zonal (u) components of drifter-measured velocity is just 10% of the meridional (v) components on average, indicating that the ageostrophic components of the flow in the LH are generally far more meridional than they are zonal when being measured by drifters. This is likely due to the times of year that the LH traps drifters, as the LH traps drifters primarily while it circulates in place in either the SC (Figure 4a) or off the southwest Indian coast (Figure 4c). These stationary periods coincide with the most intense periods of the summer and winter monsoons, respectively. During these times, the meridional winds are at their zenith, and, as such, the ageostrophic components of the flow will likewise be more meridional than zonal in nature.

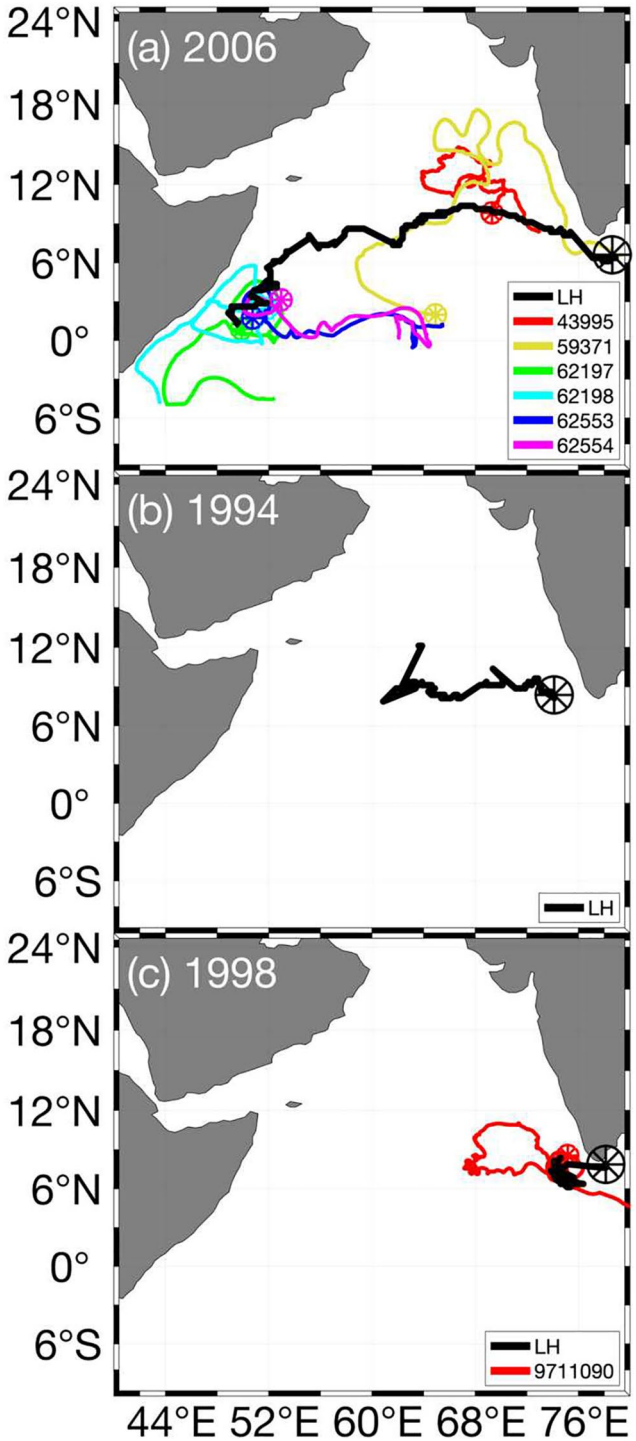

Figure 4. Trajectories of the tracked Lakshadweep High (LH) in 2006 (a), 1994 (b), and 1998 (c). Solid black lines indicate LH trajectories, while black pinwheels indicate LH origin location. Thin colored lines each correspond to a unique GDP drifter that overlapped with the radius of LH for at least a week at some point in its life. Small colored pinwheels represent the origin points of the respective colored drifter.

3.2. LH Formation & Post-Formation Characteristics

Similarly to the conclusions presented by Shankar and Shetye (1997) and Bruce et al. (1998), we find that the initial formation of the LH can be attributed to remote forcing, specifically the arrival of the second annual downwelling CKW in late November and early December (Figure 5). The composites clearly demonstrate the propagation of a high in SLA propagating around the BoB, past Sri Lanka, and arriving in the Laccadive Sea in mid-November. Of particular note is the difference in the average strength of the arriving high in late November and early December. This high extends between the southern tip of India and Sri Lanka first in full years (Figure 5c) and then in half years (Figure 5j), but is never fully formed in local years (Figures 5o and 5p). It is at this time in early to mid-December that the LH typically forms (Figures 5d, 5j, and 5p). The full year CKW continues to extend further to the northwest than half or local years' CKWs through January (Figure 5e), before expanding slightly westward toward the end of January (Figure 5f). While this extended area is present in half years as well (Figures 5k–5l), it is nearly entirely absent in local years (Figures 5q and 5r). Instead, the SAH is elevated in January of local years. Statistically, the correlation between the yearly date of maximum SLA at the entrance to the Laccadive Sea at 80°E (the right side of the box in Figure 5) and the formation date of LH is significant ($p < 0.05$). This in conjunction with the appearance of the LH in early December (Figures 5d, 5j, and 5p) supports the hypothesis that the timing of the onset of the second annual downwelling CKW is intrinsically related to the formation date of the LH.

To quantify the relationship between the extent and strength of the CKW and the formation of the LH, we have extracted the anomalies of SLA and elevated SLA area within the LH formation area, i.e., the black boxes annotated in Figure 5 (showed in Figure 6). We find that the early November amplitude of the area is roughly equivalent between full and local years before diverging in mid-December (Figure 6a). After early December, full years are always greater in amplitude and extent than local years (Figures 6a–6d). This represents the strongest section of the CKW (Figures 5d, 5j, and 5p) and reflects the results in Figure 5. Half years, however, are more variable, with peaks and troughs that can bring half years above full years (late January of Figure 6a, December through January of Figure 6d) or below local years (February of Figures 5b and 5d). That said, half years typically remain above local years and are generally similar to full years. Due to the consistently below-mean amplitudes and extents of local CKWs, we suggest that the less intense CKW is a major factor leading to the differentiation between full/half years and local LH propagation types.

Our assessment of the CKW in the Laccadive Sea both mirrors and contrasts other studies of CKWs in the Indian Ocean. For example, Rao et al. (2010), the study from which the 10 cm SLA threshold is taken, classifies 1997 as one of the weakest years in terms of equatorial Kelvin wave strength. As the CKW in Figure 5 originates in the previous year, their 1997 equatorial Kelvin wave is the wave that splits into the CKW that generates 1998 LH here, and so it follows that a weaker equatorial Kelvin wave produces a weaker CKW and weaker LH. Similarly, they classify several of our other local and half years as "weak" (e.g., 1994 and 2004) and several of our full years as "strong" (e.g., 1996 and 2000). However, for each year classification that is in agreement, there is another classification that is not in agreement (e.g., our 2005–2007 years are all full years, while their 2005–2007 years are all either

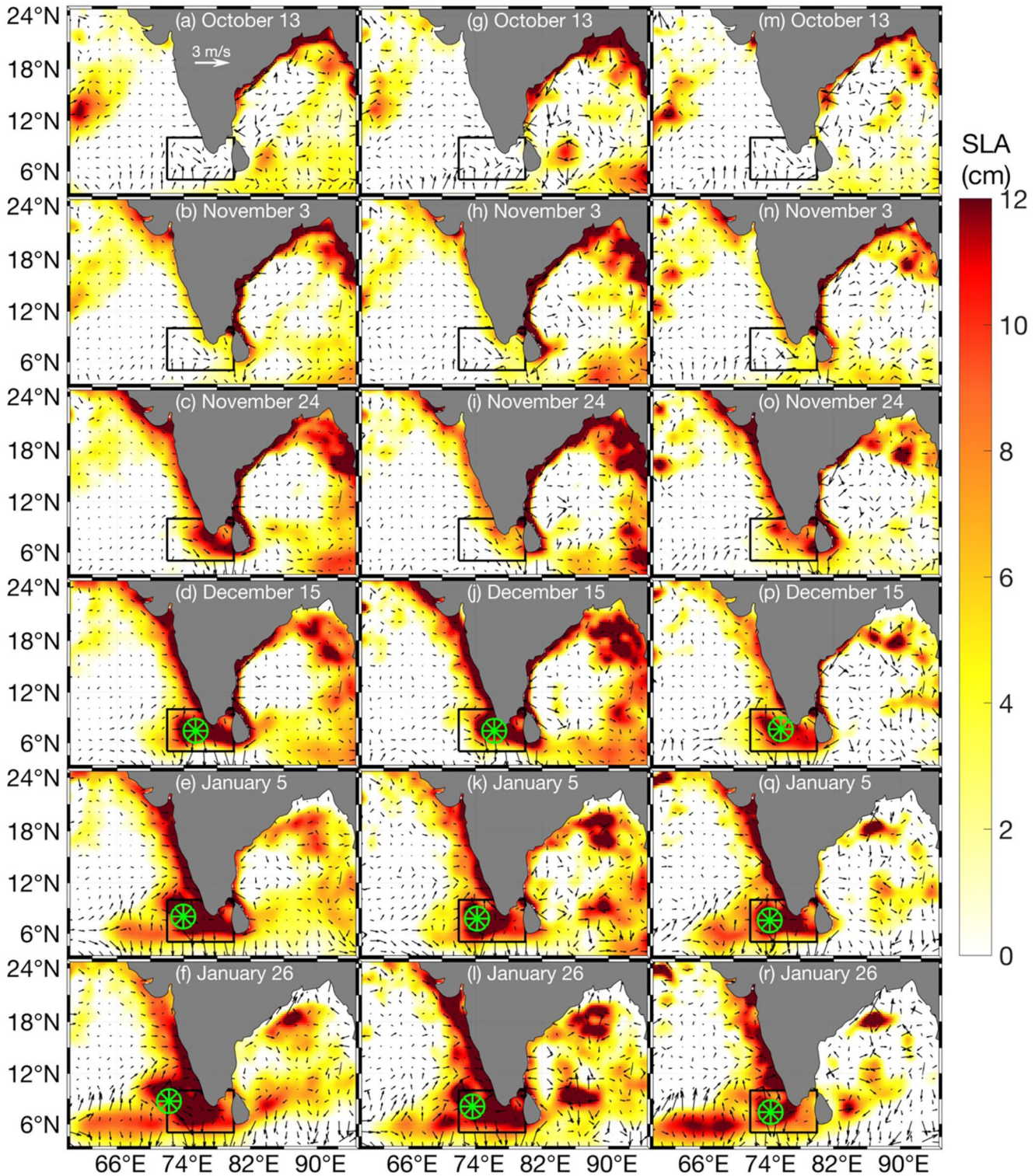

Figure 5. Sea level anomaly (SLA) (cm) depicting coastal Kelvin wave propagation between 13 October and 26 January averaged from 1993 to 2019. Arrows depict geostrophic current vectors (m s^{-1}) from altimetry data. Green pinwheels mark the average locations of the tracked Lakshadweep High (LH) at the given times. (a–f) Average for full years. (g–i) Average for half years (m–r) Average for local years. The black box is the zone within which all LHs form.

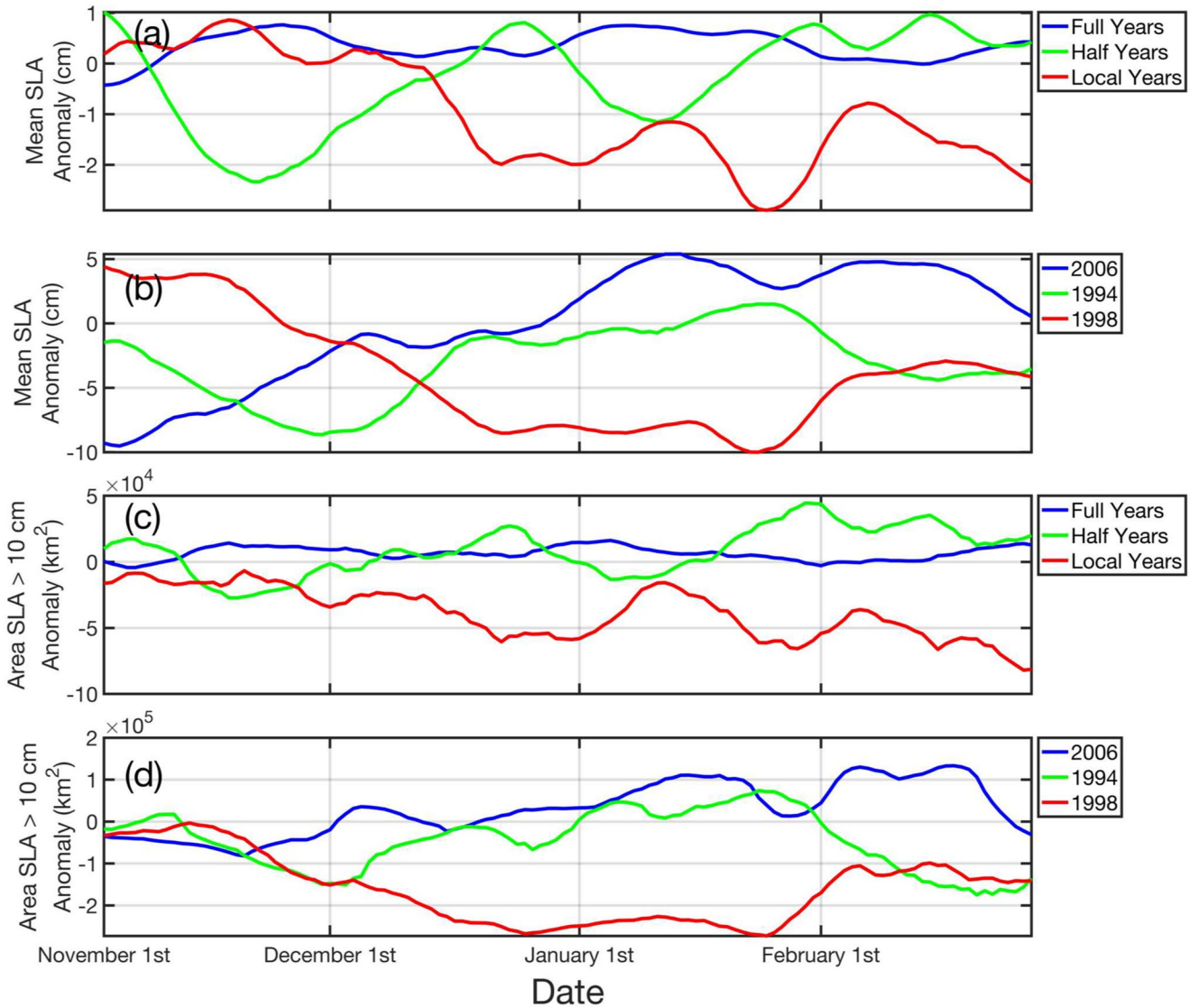

Figure 6. Mean Sea level anomaly (SLA) (cm) for all years (a) and example years (b); areas of elevated SLA (>10 cm, km^2) for all years (c) and example years (d). Means are performed over the boxed area in Figure 5 (9.5°N, 5°S, 80°E, and 72°E) and anomalies are calculated for each location in regard to a 27-year mean.

"weak" or "IOD", i.e., absent). Therefore, our results relating to the apparent strength of the second downwelling CKW in the Laccadive Sea require an additional analysis besides the original equatorial wind forcing of the Kelvin waves to explain their interannual variability.

For this additional analysis, we look to Suresh et al. (2016), who demonstrated the role of wind forcing over the southern tip of India and Sri Lanka ("STIP") and hypothesized its role in the formation of the LH. We plot the wind stress and SLA in this region in Figure 7. We find that there is a general agreement between full and half years for the entire period (Figures 7a–7f and 7g–7l) in both wind stress and SLA. However, there is a notable difference between full/half years and local years (Figures 7m–7r) especially in late November (Figures 7d, 7j, and 7p) and late December (Figures 7f, 7l, and 7r). This additionally manifests in the form to a higher SLA to the west of the STIP region.

We calculate in Figures S2 and S3 in Supporting Information S1 the lag correlation between the wind stress over the STIP region, both as in Suresh et al. (2016), and in the area between 5°N, 9°N, 76°E, and 80°E as in Figure 7. We find that the strongest correlations between wind stress in the latter region and SLA in the LH region occur at a 30–60 days lag (Figures S3e–S3f in Supporting Information S1), with significantly higher correlations in

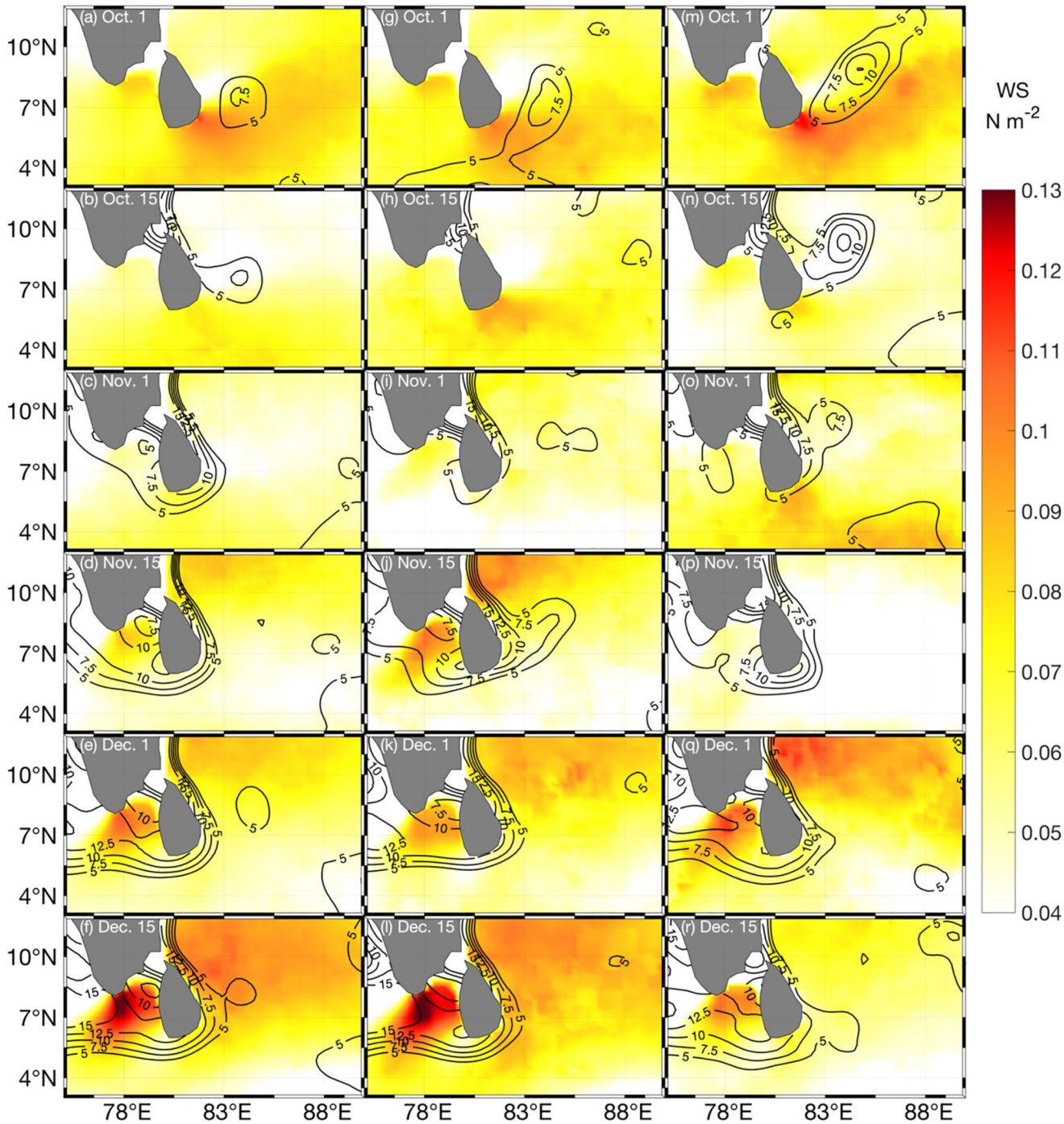

Figure 7. Mean wind stress (N m^{-2}) and Sea level anomaly (SLA) contours over the southern tip of India and Sri Lanka (STIP) area between the beginning of October and the end of December for full (a–f), half (g–l), and local (m–r) years. Each date represents the beginning of a 2-week period over which the wind stresses and SLAs are averaged.

full years than in either half or local years (Figures S3l–S3m and S3s–S3t in Supporting Information S1). This suggests that the wind forcing in the STIP region contributes more heavily to the post new year phase of LH development in full years than in either other type of year. As a result, differences between full, half, and local years lie not just in the amplitude of the CKW, as in Figure 5, but also in the wind stress in the STIP region prior to the new year.

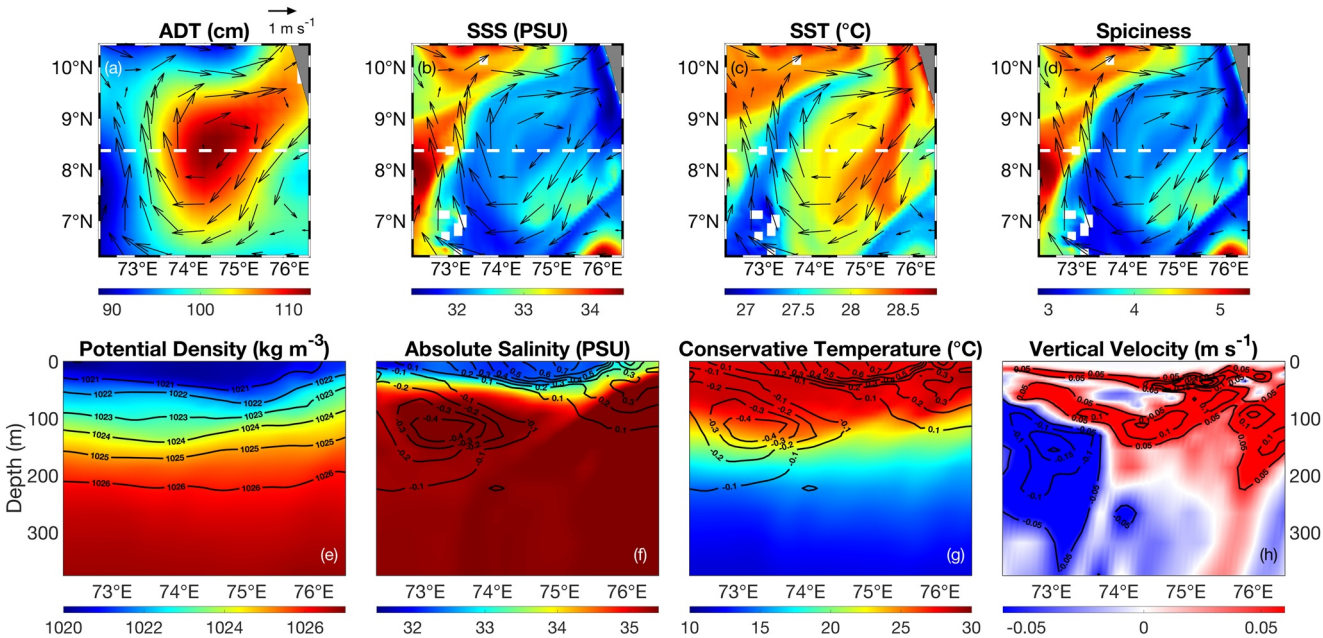

Figure 8. The 3-dimensional profiles of the location and date marked by the black pinwheel in Figure 3a for the full example year (15 January 2006). These are as follows: (a) measured absolute dynamic topography (ADT) (cm), (b) GLORYS12v1 sea surface salinity (SSS) (PSU), (c) GLORYS12v1 SST (ºC), and (d) Spiciness with geostrophic current vectors overlaid. The white dashed line depicts the cross sections of the following properties: (e) Potential density (kg m^{-3}) with isopycnals overlaid. (f) Absolute salinity (PSU) and (g) conservative temperature (ºC) with contours of swirl velocity (m s^{-1}, meridional components) overlaid. (h) Vertical velocity (m s^{-1}) with its own contours overlaid. White squares represent regions of no GLORYS12v1 data, in this case representing the Lakshadweep islands.

We now examine the three-dimensional structure of the LH, beginning 1 month after its formation in 2006 (Figure 8). The 2006 full LH's core amplitude at this stage is 112 cm (Figure 8a), and it is entraining fresher BoB water into its core from the south, with a core sea surface salinity (SSS) that is 3.1 PSU fresher than the northwestern flank of AS water (Figure 8b). This entrainment is similarly visible in the surface temperature profile (Figure 8c). The difference in the surface spiciness of the two masses confirms that it is SSS and not SST that is the dominant property separating BoB water from AS water (Figure 8d). The lens of BoB water extends to a depth of approximately 50 m before the saltier AS water dominates below the halocline (Figures 8e and 8f). The vertical extent of the BoB water is consistent with studies of winter monsoon transports in the region, which confirm that BoB water transported around Sri Lanka is limited to the upper 100 m of the ocean (Schott et al., 1994). The depth of the BoB water is also visible in the depth of the thermocline, as the temperature remains relatively uniform down to 90 m (Figure 8g). There is strong upwelling on the eastern side of the eddy, with a region of subsurface downwelling to the west (Figure 8h). This pattern of western downwelling and eastern upwelling is consistent with the modeling of Rao et al. (2008), namely their Figure 12, which displays a similar region of downwelling corresponding to the western flank of the LH. As noted by Rao et al. (2008), this downwelling can be expected to move westward along with the LH in full and half years.

The center amplitude of the 1994 half LH is comparable to but less than the full LH at 106 cm (Figure 9a). The half LH is also further to the northwest as compared to the full LH and so the salinity and temperature signatures of the BoB water is shifted to the south relative to the center of the LH (Figures 9b–9d). A filament of the AS water is pulled around the northern edge and into the core of the LH from the east, swirling and mixing together with the BoB water from the south and southeast. This results in a less pronounced fresh lens, with the lower density BoB water being shifted to the west of the center of the LH (Figures 9e and 9f). The temperature profile is similar to the full LH, with the exception of a small shallowing of the thermocline on the western edge. As with the full LH, positive vertical velocity dominates the center of the LH while a negative vertical velocity is seen below the surface to the west (Figure 9h).

Finally, the amplitude of the 1998 local LH is the smallest of the three LHs, achieving only 98 cm at the center (Figure 10a). Of particular note is the scale of the ADT (Figure 10a) and SSS (Figure 10b) as compared to its full and half counterparts. The entire region is nearly 10–20 cm lower in 1998 than in 2006. This is likely due to the

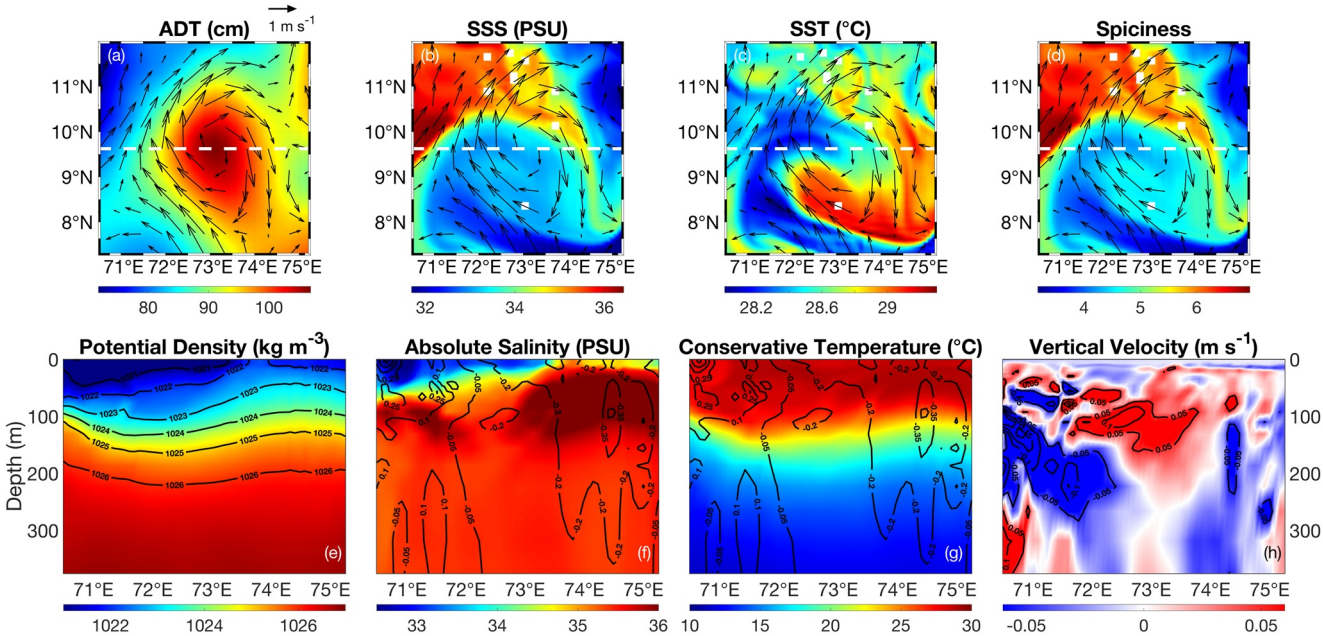

Figure 9. Same as Figure 8 but for the location marked in Figure 3d for the half example year (15 January 1994).

CKW amplitude differences discussed in regard to Figure 6. The SSS minimum is only 32.9 PSU as compared to the 31.3 PSU of 2006, and the high surface temperature signature of AS water is more prominent to the northeast of the LH (Figures 10b and 10c). These comparisons indicate that the mean flow of BoB water into the region is substantially reduced between full and local years, confirmed by the spiciness of the region, which demonstrates only a small filament of BoB water on the west coast of India (Figure 10d). The isopycnals are more clustered and the thermo- and haloclines more condensed in the local LH reflecting this comparative lack of mixing and shallowing of the mixed layer depth (Figures 10e–10g). In the same way, the up- and downwelling of the LH are both less intense than in full or half years.

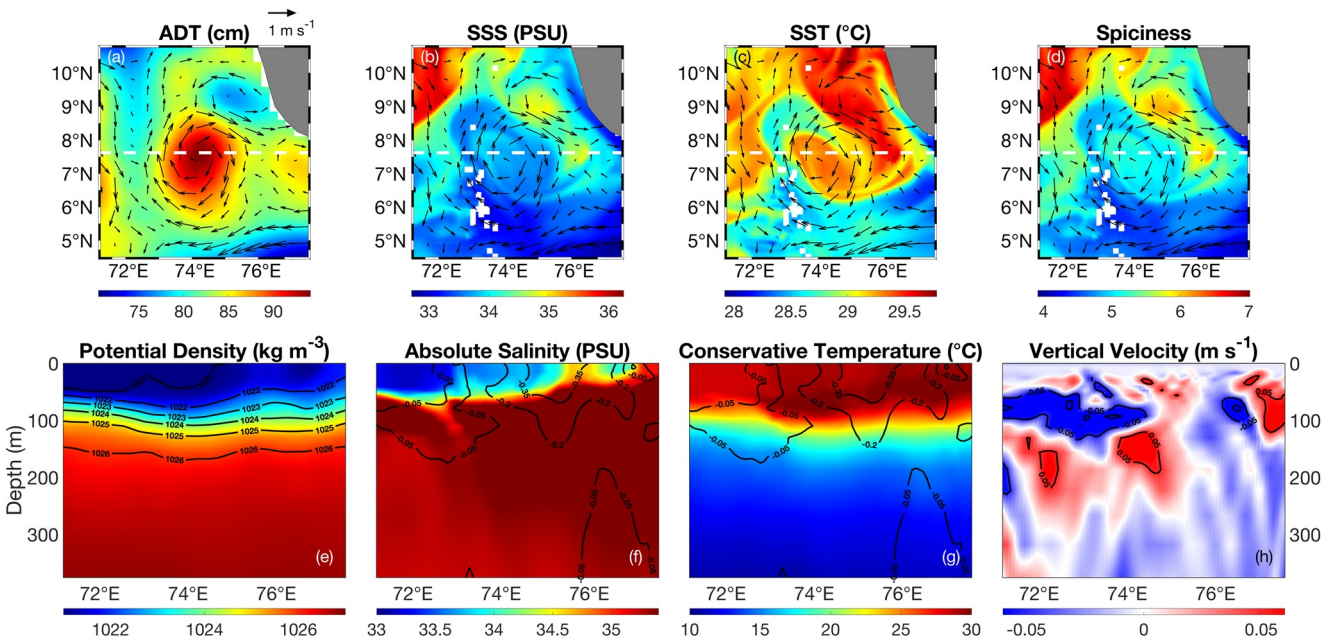

Figure 10. Same as Figure 8 but for the location marked in Figure 3g for the local example year (15 January 1998).

Contributing factors to the differences between this local LH and the full and half LHs before it include the combined 1997–1998 El Niño and fall 1997 IOD event. Durand et al. (2009) find that the East India Coastal Current flows anomalously poleward prior to the 1998 winter monsoon, while Jensen (2007) models that BoB water penetration into the AS basin during the winter monsoon should be lowered during El Niño years and entirely absent during IOD years. In 1998, these factors occur at once, combining with the smaller CKW to possibly facilitate a lower-magnitude LH. It is worth noting that the 1993–1994 El Niño/IOD event is generally a less extreme version of the 1997–1998 event (Schott & McCreary, 2001), which matches well with our classification of those years as half and local years, respectively. This analysis is complicated by the fact that ENSO/IOD modes manipulate each other and the monsoons in following years (Izumo et al., 2010; Yuan et al., 2008). Further research into the exact consequences of ENSO/IOD on the Laccadive Sea during the winter monsoons would be required to quantify the precise amount of variability in the LH due to these events.

3.3. LH Development Post-Formation

As CKWs are transient (i.e., Figure 5) and are subject to substantial interannual variability, they may fail to provide the continual energy required for the maintenance and expansion of the LH. Furthermore, we find that the elevated SLA area calculated in Section 3.2 more than doubles after the new year. In full years, this area reaches an average of 332,000, 12,000 km^2 larger than in half years and 77,000 km^2 larger than in local years. While this may be partially attributed to the wind stress in the STIP region (Figure 7), there may be other factors during this time that assist in forcing the growth of the LH. Specifically, we explore the hypothesis put forward by Bruce et al. (1998) that the expansion of the eddy field is due to strong negative WSC in the LH region over the course of the winter monsoon (Figure 11).

There is indeed a strong ($<-1 * 10^{-7}$ N m^{-3}) region of negative WSC in the average case of all modes of LH propagation in January and February (Figures 11a, 11b, 11g, 11h, and 11m, 11n). In each type, the WSC weakens around the LH after February (Figures 11c, 11d, 11i, 11j, and 11o, 11p) before increasing in magnitude dramatically with the onset of the summer monsoon in May and June (Figures 11e, 11f, 11k–11l, and 11q, 11r). It is worth noting that the full type of LH on average propagates into another region of negative WSC as the summer monsoon intensifies (Figure 11f). This may explain why the full LH deteriorates in the central AS before restrengthening as it enters the SC region, and why the half LH dissipates during the intermonsoon period (Figures 11k–11l). In order to further provide evidence for this connection, we examine the normalized point-by-point covariance for the average LH of each type during the same time period in Figure 11 (Figure 12).

We find that the normalized covariance supports the WSC hypothesis, as a negative covariance indicates that a negative WSC is forcing a more positive ADT throughout January and February (Figures 12a, 12b, 12g, 12h, and 12m, 12n). The LH is constantly in a region of significant correlation in regard to local wind forcing the ADT field during this time. Furthermore, we see that the LH as it propagates in the full and half modes seems to ride a line of exactly 0 covariance with a nonsignificant correlation (Figures 12c–12e and 12i–12k) suggesting that the eventual dissipation of the half LH is likely not caused by any active effect of the wind rather due to a lack of wind. This lack of correlation with local wind suggests the ADT field is primarily due to by non-wind forcing in this case a Rossby wave, which we expand upon in Section 3.4.

We take a closer look at the effect of the wind on LH growth by quantifying WW and the WSC alongside the radius and EKE of each type of LH over their development periods (Figure 13). The largest quantity of wind work is done over the LH during the first months of the LH's life, consistent across all LH types (Figure 13a). The effect of wind reduces over time in most cases so that the third month's wind is generally less intense than the first month's wind. We find that the full LH experiences above-average WW in the first 2 weeks of its lifespan and again around 35 days after formation (Figure 13b). We also find a strong spike in WW centered around 60 days postformation. With these spikes aside, there is little average deviation across year types. We also find that WW varies considerably within an individual year (Figure 13b). Overall, we do not find any significant correlation between amounts of wind work done and type of the LH. By contrast, the WSC manifests a very particular pattern, as negative WSCs correlate with local LHs (Figure 13c). Additionally, the net WSC over the 2006 and 1994 LHs is positive for the first 2 months of their lives (Figure 13d). Regardless of the sign of the WSC, the LH grows substantially between the first and second months before typically plateauing or diminishing slightly after its third month (Figures 13e and 13f). This decline is more sharply pronounced in the radius of half and local LHs than in full LHs. The end result is that the radii of full LHs are generally comparable with the radii of half LHs and

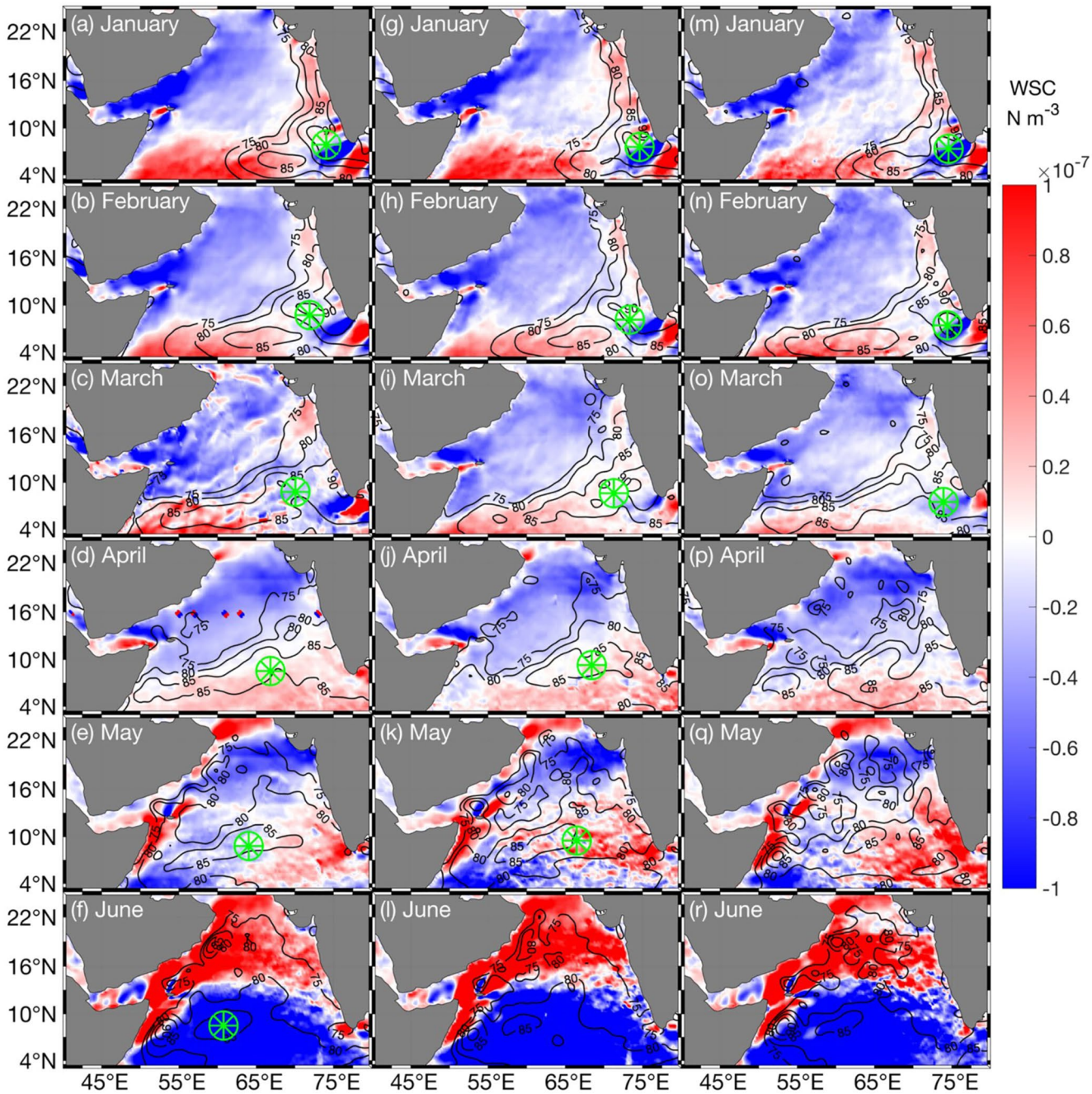

Figure 11. Wind stress curl (WSC) (N m^{-3}) for the first week in each month between January and June averaged from 1993 to 2019 in the Arabian Sea. Contours depict areas of elevated absolute dynamic topography (ADT) in intervals of 5 cm. Green pinwheels mark the average locations of the tracked Lakshadweep High (LH) following the trajectories marked in Figure 2. (a–f) Average for full years. (g–i) Average for half years (m–r) Average for local years.

significantly larger than the radii of local LHs at the end of the growth period. This mirrors the end state of EKE (Figures 13g and 13h), where both the full LH and the 2006 LH lie substantially above the average as compared to the below-average performance of half (1994) and local (1998) LHs. If the LH were being directly grown through the negative WSC, then the opposite would be expected, as the local/half LHs receive a more negative WSC and a similar amount of WW to full LHs.

A possible explanation for this lies in the recent work by Rai et al. (2021) that demonstrates that the wind extracts more energy than it inputs into the small scale circulations across the global oceans, a phenomenon dubbed "eddy

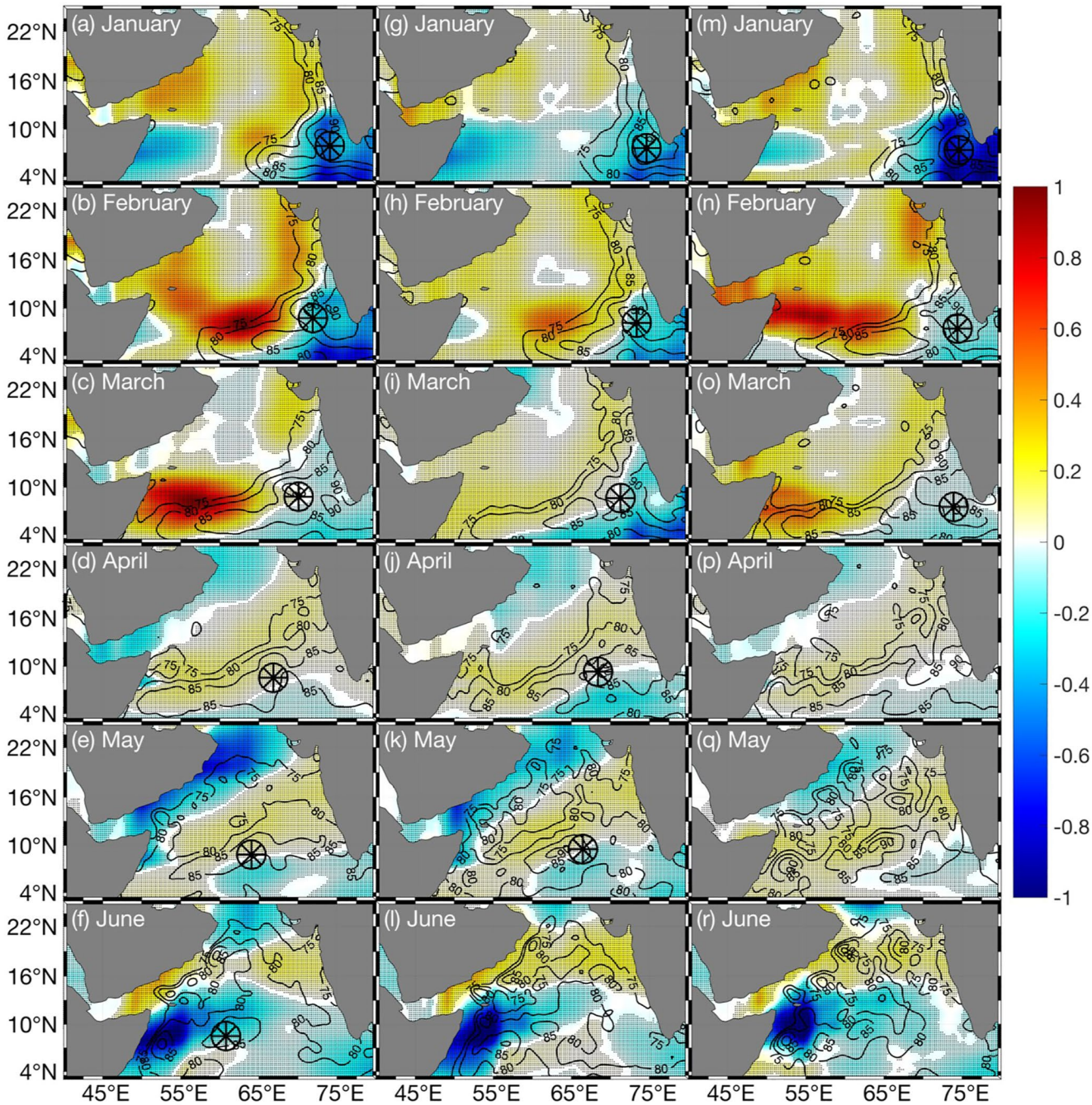

Figure 12. Same as Figure 11, but displaying the normalized spatial covariance between the wind stress curl and the absolute dynamic topography. Areas of significant correlation ($p < 0.05$) are shaded.

killing." As the individual LH eddy is rarely larger than their threshold for small-scale circulations (260 km), it would follow that the wind is actually "killing" the LH, rather than enhancing it as expected. Even with this eddy killing effect, the wind would still be simultaneously energizing the large-scale circulation of the Laccadive Sea, forcing Rossby waves within the region as concluded by Brandt et al. (2002). These large-scale Rossby waves would then explain the growth of maintenance of LH, as we demonstrate in Section 3.4 that the LH is carried along them. However, the relative amount of energy taken from the LH by eddy killing as compared to the energy entered into LH by the forcing of Rossby waves remains unclear. This warrants further research into how eddy killing changes over the course of the monsoons, but this is outside the scope of the present study.

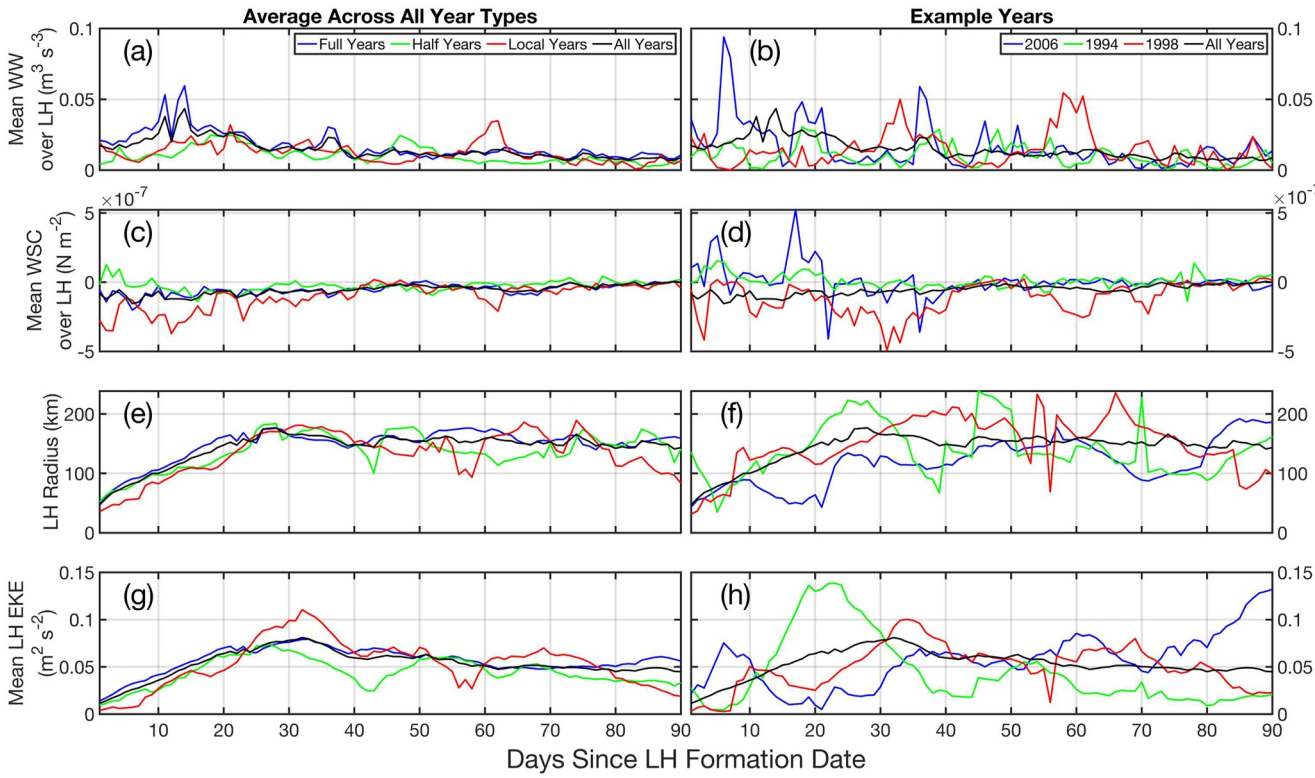

Figure 13. The characteristics of the Lakshadweep High (LH) and the wind over the radius of the LH for the first 90 days of its lifespan for each year type (left) and example years (right): (a) is the mean WW ($m^3\ s^{-3}$) for all propagation types; (b) is as in (a) but for example, years; (c) is the mean WSC ($N\ m^{-2}$) for all propagation types; (d) is as in (c) but for example, years; (e) is the radius (km) of the LH for all propagation types; (f) is as in (e) but for example, years. Lastly, (g) is the mean EKE ($m^2\ s^{-2}$) of the LH for all propagation types; (h) is as in (g) but for example, years. Black lines display the average for all years and are the same across both columns.

We also find that, both in the average (Figure S1a in Supporting Information S1) and the example years (Figure S1b in Supporting Information S1), the LH experiences frequent spikes and average higher values in terms of nearby mesoscale eddies over the first 3 months of its life. This, combined with observations of the half and local LHs, indicates that these propagation types undergo more extensive splitting events during their growth periods. This provides another way for the half and local LHs to diminish by transferring energy from the mesoscale to the submesoscale. Algorithms specifically tailored to the splitting and merging of eddies, e.g., Tian et al.'s (2021) *EddyGraph*, are currently being developed and may be used to more specifically quantify the effects of these processes on the LH. Additional submesoscale measurements, such as those collected from the NASA Surface Water and Ocean Topography (SWOT) mission, will also help elucidate this process of energy transfer.

We close this section by suggesting that local years are the minority of total years because they require both a weak CKW (Figure 5) and a greater diminishing of the LH specifically due to the effect of the wind (Figure 13) and by eddy splitting (Figure S1 in Supporting Information S1) as compared to full years, which represent a relatively normal or strong state of CKW propagation and normal or weak WSC in the eastern AS.

3.4. LH Propagation

While we have since investigated both the formation and developmental mechanisms and the variability of those mechanisms with respect to the LH, we still need to address its westward propagation using a Hovmöller diagram (Figure 14). The propagation of the LH is, on average, latitude restricted between the bounds of 7°N–9°N (Figure 2).

The typical propagation of Lakshadweep High (LHs) is restricted to a band of high SLA, rarely leaving the 10-cm contour defined in Section 3.2. Even in half and local years, this contour extends across the basin (Figures 14b and 14c). We also note that the width of this contour is narrower around March in local years (Figure 14c), as it

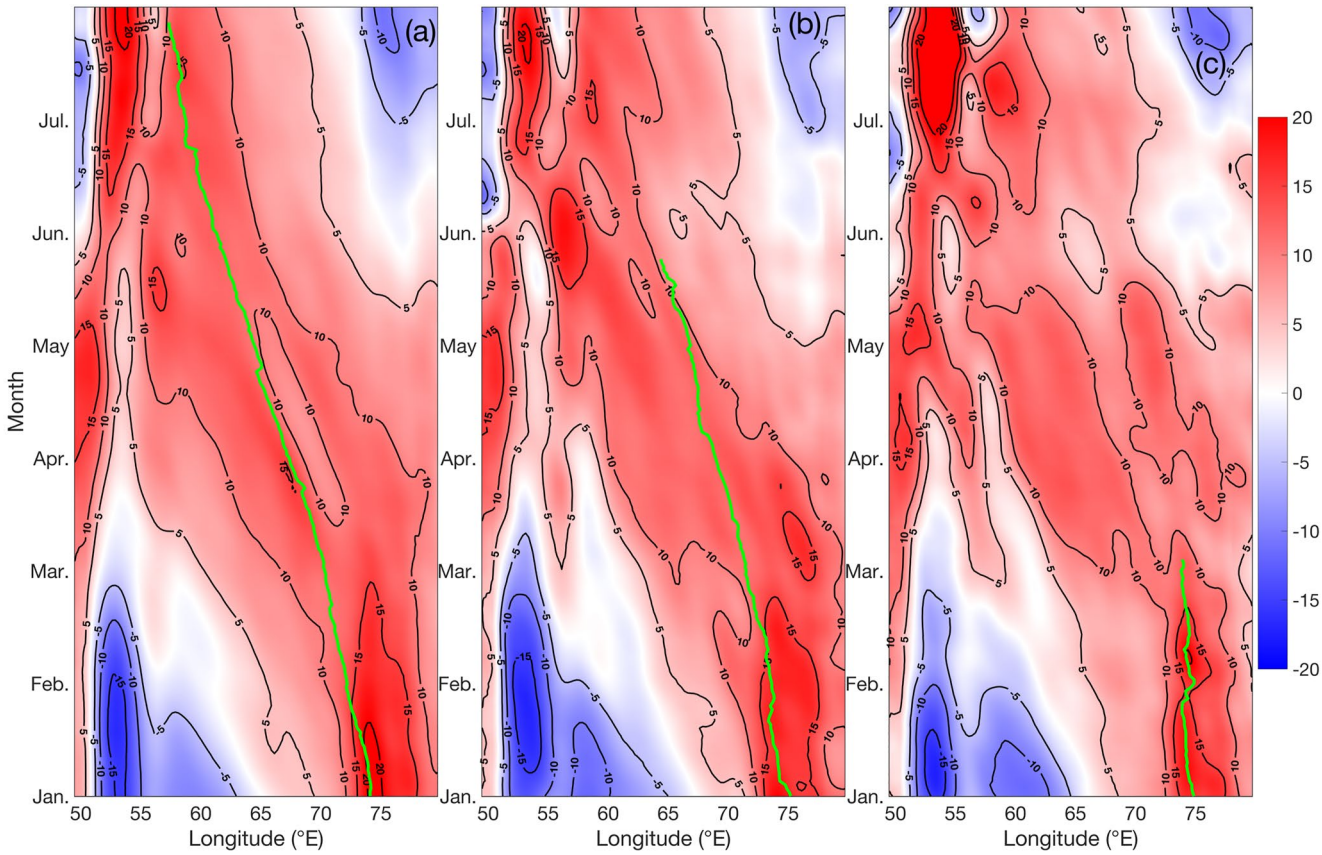

Figure 14. Hovmöller longitude-time diagram of sea level anomaly (cm) contours for a spatial average of 7°N–9°N and a temporal average for 1993–2019 between January and the end of July. Green lines depict average Lakshadweep High propagation (see Figure 2) along this longitude: (a) Average for full years, (b) average for half years, (c) average for local years.

diverges from the average path of the LH. These two factors together demonstrate that this westward propagating high is independent of the participation of LH, but increases in magnitude when the LH propagates with it.

In order to confirm whether or not the propagation of LH is a fundamental aspect of the first downwelling Rossby wave, we perform a RT on the L/T plot in Figure 14 (Figure 15).

According to the maximums in the standard deviations of the transform, we find that the corresponding degree of rotation is between 6° and 7° (Figure 15d) and that the resulting Rossby wave phase speed is between 11.13 and 13.37 cm s^{-1} (per Equation 3). This reasonably matches the observations and theoretical calculations of previous studies along this same latitude band (see Subrahmanyam et al. (2001) Table 4). Furthermore, upon taking the location of the average full LH on March 1st and its eventual destination when it terminates in late July (Figure 14a) and calculating the distance it travels divided by the time it takes to propagate, we find an average propagation speed of around 12.1 cm s^{-1}. Given that the two speeds align, we suggest that the LH's propagation across the AS basin is due primarily to a Rossby wave bound to 8°N. The mechanism for this propagation may be as presented by Polito and Sato (2015), who demonstrated that the phase speeds of eddies and Rossby waves will tend to align such that an eddy "rides" Rossby waves. This speed alignment occurs due to an out-of-phase eddy being forced by an asymmetric divergence field toward the Rossby wave crest and functions primarily in situations where an eddy and a Rossby wave are locked in phase for large durations, such as the LH transiting across the AS.

As noted earlier, the strength of this Rossby wave is largely attributable to the same factors as LH, i.e., the initial CKW and the subsequent WSC over the region (Brandt et al., 2002). Due to this, it would follow that a weaker LH would be less likely to accompany a weaker Rossby wave. A smaller LH in local years may also fail to propagate due to needing to pass through the Lakshadweep islands and over the Chagos-Laccadive Ridge. The LH

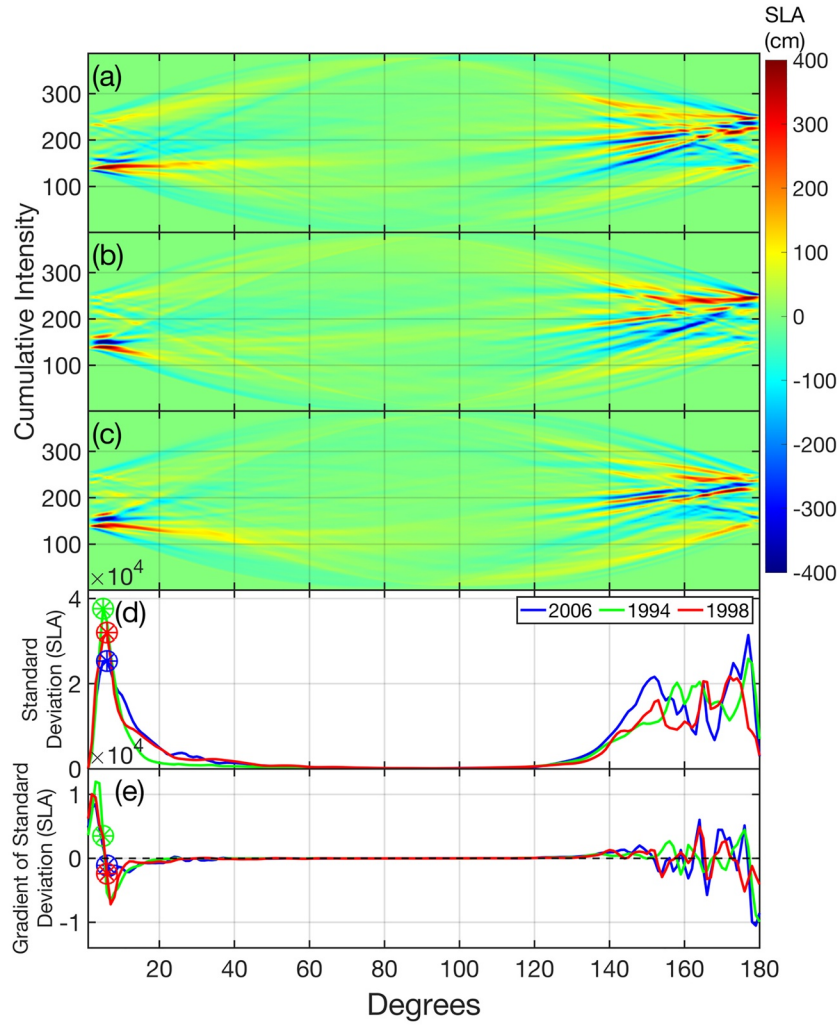

Figure 15. Radon transforms of the L/T plots shown in Figure 14: (a) Transform for full years, (b) transform for half years, (c) transform for local years, (d) is the standard deviation of the SLA in (a–c) on blue, green, and red lines, respectively. Colored pinwheels mark the maximum in the curve, (e) plots the gradient of (d).

may then remain trapped behind the ridge. The exact effects of the Lakshadweep islands on the eddy field around them is unstudied, but as the LH is in the lee of the islands during the winter monsoon, it is possible that their presence enhances the EKE of the LH in a similar manner to that demonstrated by Calil et al. (2008). This could bolster the local LH until the end of the winter monsoon, which is indeed what we observe, as the local LH in 1998 persists into March.

We continue our examination of the LH structure over time in each of its modes, beginning with a snapshot of the full type in late March of 2006 as it propagates (Figure 16). At this point in time, the full LH has traveled 780 km west and 190 km north from its position in Figure 8. We find that, even as the full LH is no longer affected by the local WSC (Figure 12c), the LH remains remarkably coherent after it passes 70°E with an amplitude of 103 cm (Figure 16a). Its low-salinity lens has been carried with it but is less than 40 m deep and has been eroded at its minimum from 31.5 PSU to 33.5 PSU (Figures 16b and 16f). This is reflected in the difference between the low core density of the LH and the high density of surrounding AS water (Figure 16e). The spiciness profile confirms that this is still an exchange of water masses dominated by differences in salinity (Figure 16d) as temperature is still largely comparable across the eddy (Figures 16c and 16g). Lastly, the vertical velocity profile is similarly eroded and not nearly as pronounced near the surface as earlier in its life cycle (Figure 8h). Regardless, at this point, the 2006 LH is still strongly defined in relation to its surroundings.

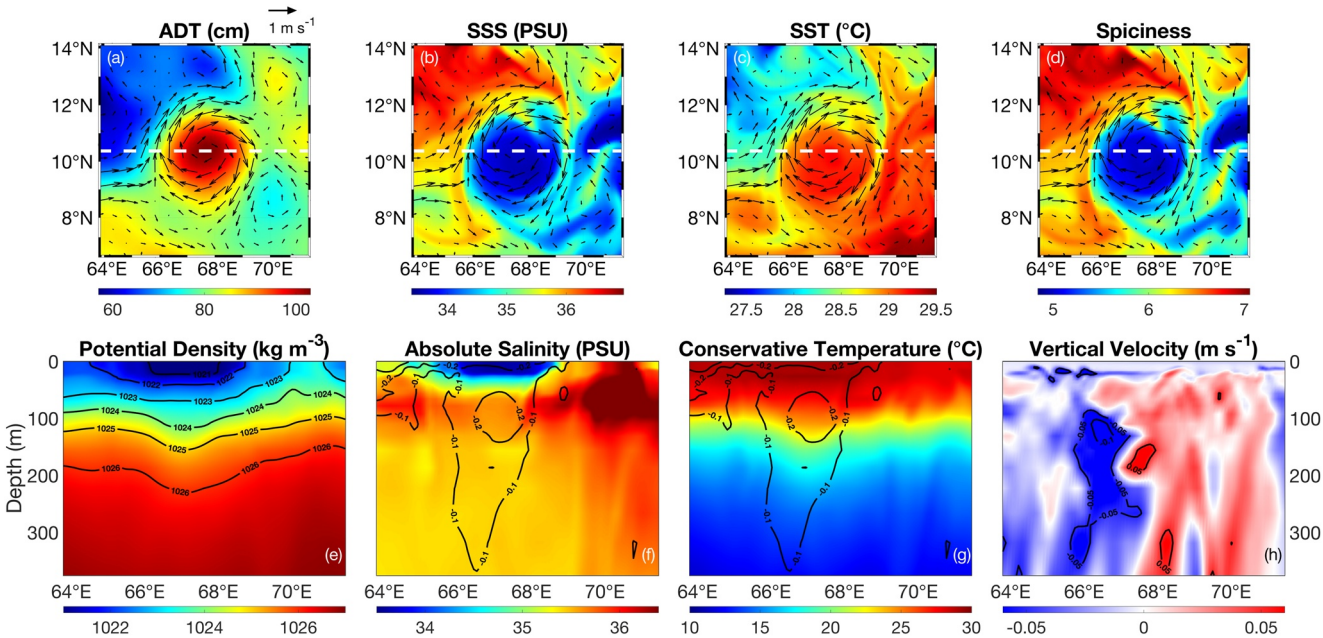

Figure 16. Same as Figure 8 but for the location marked in Figure 3b for the full example year (26 March 2006).

This may be contrasted with the profiles of the 1994 LH (Figure 17), which present an eddy close to decoherence. The half LH here has traveled slightly further westward as compared to the full LH (890 vs. 780 km) and instead of propagating northward, it has instead moved southward by 140 km. The ADT amplitude of the half LH is still pronounced, achieving over 90 cm at its center, but this high is shared with smaller eddies to the southeast and southwest (Figure 17a). The geostrophic current vectors around the LH are already flowing into these eddies, facilitating an exchange that is visible in the SSS profile (Figure 17b) and the SST profile (Figure 17c). Here, relatively low salinity water is transported from the southwest into the center of the LH before being carried around the eddy center and into the southeast eddy. For the first time, the spiciness profile displays characteristics

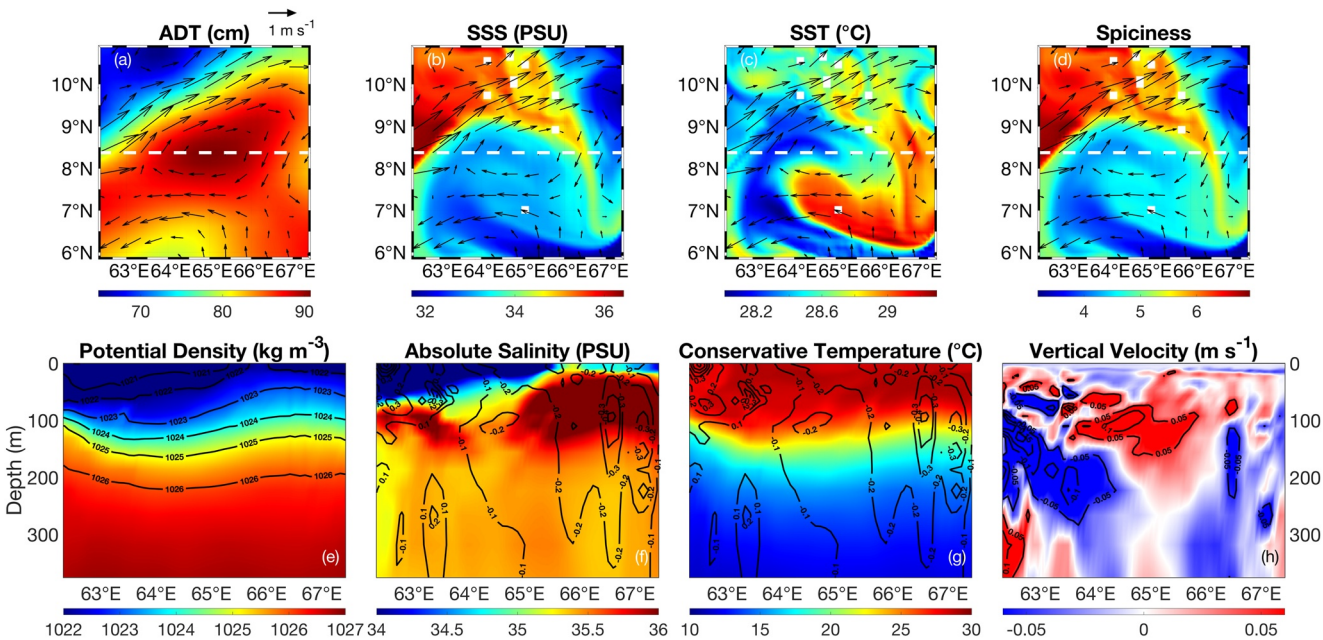

Figure 17. Same as Figure 8 but for the location marked in Figure 3e for the half example year (26 March 1994).

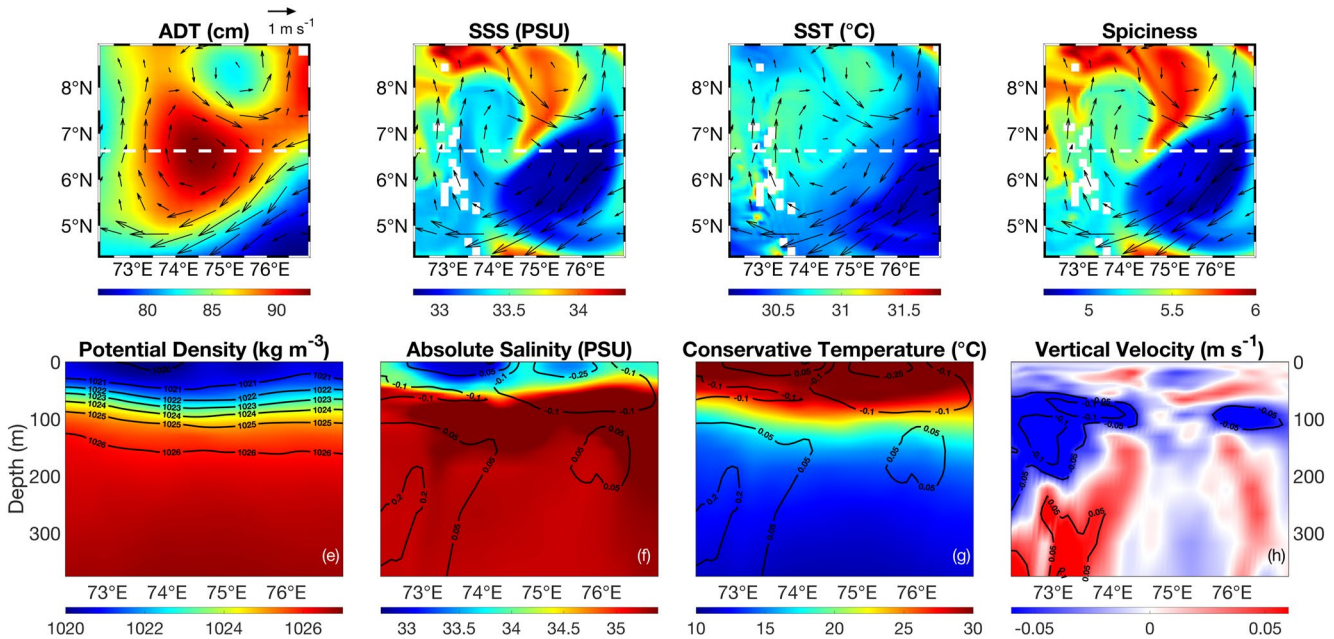

Figure 18. Same as Figure 8 but for the location marked in Figure 3h for the local example year (26 March 1998). As before, white squares mark the locations of the Lakshadweep islands, which are not painted over in the GLORYS12v1 data set as they are in the Copernicus Marine Environmental Service (CMEMS altimetry interpolations.

of both the mixing of salinity and temperature, though the salinity profile still dominates (Figure 17d). The LH eddy center has been meridionally compressed, and carries only a very shallow, less than 30-m deep contour of approximately 34 PSU water that is similarly visible in the density profile (Figures 17e and 17f). While there is still a column of positive vertical motion to the eastern side of the LH (Figures 17g and 17h), this eddy is otherwise close to splitting. In fact, a week after this snapshot, it will splinter into the eddies around it, although its core maintains coherence as a substantially smaller eddy for several months. This core, now with less than 50 km in radius, repropagates eastward and then northward before finally dissipating on June 10th (Figure 4b).

Lastly, we examine the fate of the 1998 local LH, which has only shifted 110 km south and 55 km east since it was last examined in Figure 10 (Figure 18). As with the half LH, the local LH is beginning to lose coherence amidst other eddies (Figure 18a). Its geostrophic current vectors also begin to flow into these competing eddies to the north and northeast. However, due to its proximity to the west coast of India, it still maintains a relatively fresh core of under 33 PSU that is prominent in the near-surface density profile (Figures 18b, 18e, and 18f). This fresher water is being supplied from the east along a relatively strong current, a remnant of the winter monsoon current. Beyond this fresh core, the temperature across the LH is near uniform, with only minor differences about a mean of 31°C (Figures 18c and 18g). As a result, the spiciness profile again reflects salinity primarily (Figure 18d). The vertical profile lacks any kind of centrally occurring pattern, with a negative column overlying a positive column to the west (Figure 18h). As with the half LH of 1994, this eddy will dissipate soon merging with the northern eddies and losing coherence in its core on April 11th.

3.5. Effect on Somali Current

Even after the half and local LHs have decohered, the full LHs continue to approach the SC region, possibly bolstered by the WSC prior to and during the onset of the summer monsoon (Figure 11f). Therefore, we next examine the changes in the SC region that result from the different modes of propagation of LH (Figure 19).

Here, the SC region is defined as the area between the Equator, 11°N, 40°E, and 58°E (similar to de Marez et al., 2019, Figure 5a, area B). We immediately find that there is a large spike in all median eddy characteristics at the end of August in 1998, followed by a sharp decline, and then another spike (Figure 19c). Due to the median being used for this analysis, this indicates that there is a merging of eddies (the first spike), followed by a major splitting event (the dip), and concluded by another major eddy merger (the second spike). This hypothesis is

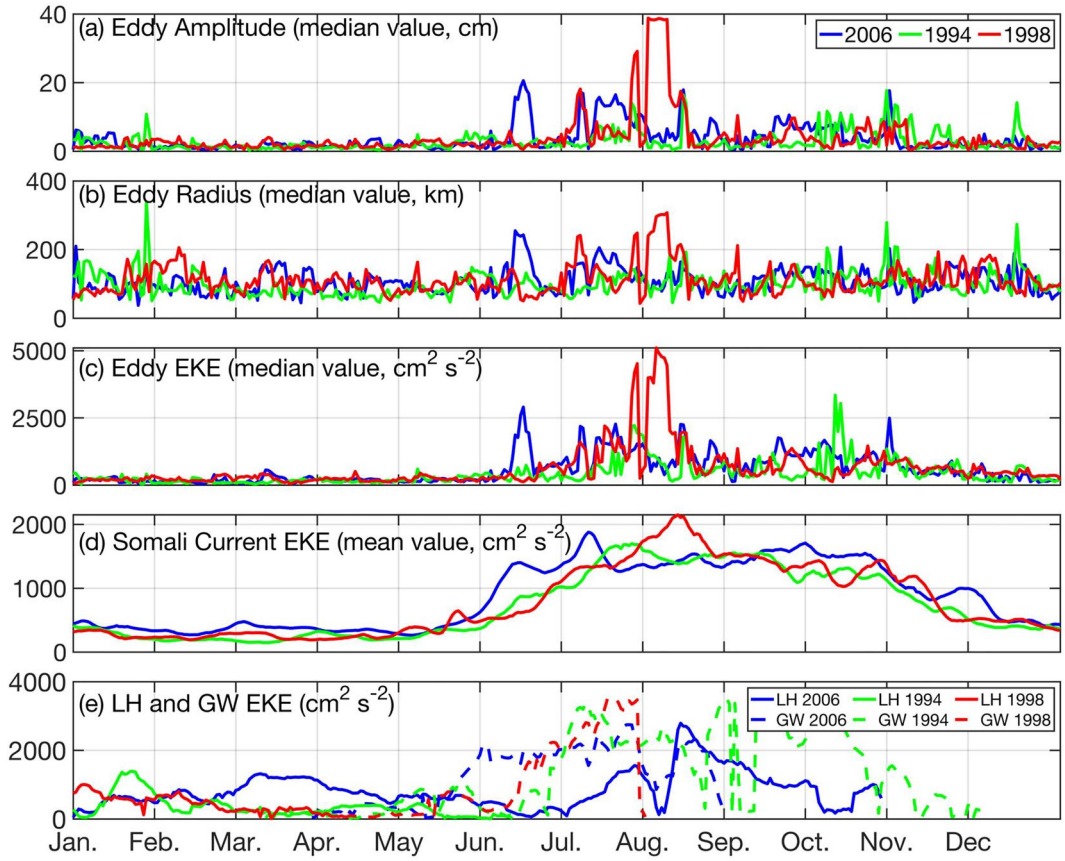

Figure 19. Yearlong characteristics of eddies in the Somali Current (the area between the Equator, 11°N, 40°E, and 58°E) for 2006, 1994, and 1998. Characteristics include the spatial median Somali Current (SC) eddy (a) amplitude in cm, (b) radius in km, and (c) eddy kinetic energy (EKE) in cm^2 s^{-2}. (d) Mean EKE of the SC from geostrophic current observations. (e) EKE in cm^2 s^{-2} of the Lakshadweep High (LH) (solid lines) and GW (dotted lines) of each year. The GW is tracked in the same way that the LH is as set out in Section 3.1, but for the SC region and April through June.

supported by the abrupt apparent dissipation of the original tracked GW at the beginning of July, simultaneously with the dip in median eddy characteristics. In effect, the GW undergoes a rapid series of splittings and mergers, with the resulting GW emerging even stronger for the first weeks of August. However, these August spikes are almost entirely absent in 2006 and 1994, and the high in the SC EKE continues after the GW has reached its zenith (Figure 19d). The only other major spikes are those in the properties of the SC eddies in mid-June of 2006 and in the SC EKE in mid-early July (Figure 19d). An examination of the ADT of the region over time reveals that this first spike is largely attributable to the arrival of the forward elements of the 8°N Rossby wave, while the second spike is the arrival of LH itself. The dip shortly afterward is due in part to the ejection of the GW from the defined SC region.

In regard to the full-lifetime LH EKE profiles (Figure 19e), we find that the main divergence between 2006, 1994, and 1998 occurs in early March, with the full LH emerging as more than twice as energetic as the half or local LH. In addition, the 2006 LH is the only LH of the three here that begins a second period of growth, as it enters the SC region in July. It is worth noting here that the dissipation dates of all half LHs are clustered around a mean of May 23rd, with the latest date being June 23rd and the earliest date being May 5th. In all circumstances, the half LH dissipates either by merging (splitting) with (into) several nearby eddies, as in 1994 (Figure 16), or by slowly reducing in size until it is no longer defined, as in the year 1999. In each case, the LH dissipates before the maximum of the southwest monsoon is reached (Figures 11k and 11l). Given the matter of a month until the southwest monsoon peak revitalizes the full LH (Figure 19e) as noted above, the difference in strength between the full and half LHs is just enough to fail to sustain the half LH until this latter period of growth.

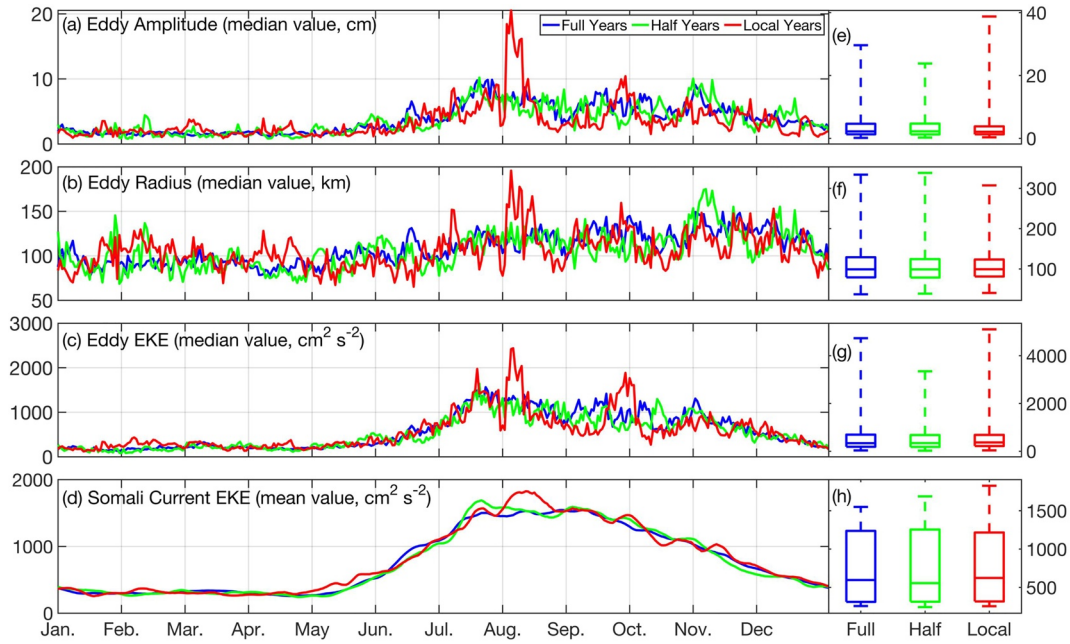

Figure 20. Same as Figure 19 but averaged across all years 1993–2019 (e–h) boxplots with the mean, upper and lower quartiles, and minimum and maximum of the characteristics shown.

Of additional interest in Figure 19e is the decline of the GW in late August of 2006. This occurs due to the GW traveling northward at the same time as the LH enters the SC from the east. The LH then remains stationary in the SC in the GW's previous location until it dissipates. After one last spike in EKE in mid-August, the GW rapidly diminishes and dissipates by September, while the LH slowly decreases in EKE until the end of October. Although not the usual case for LH across all years surveyed, this type of event where the GW rapidly diminishes as the LH grows larger in the SC did occur five times over the period surveyed, in 2000, 2006, 2007, 2014, and 2017 (the eddy identified as the LH in 2000 is notable for being additionally identifiable as the SAH, GW, and Socotra Eddy at different points in its more than year-long lifespan, a unique feat among all eddies surveyed).

In order to determine if the changes in the SC by type of LH are robust, we survey the average characteristics of the SC region over all years (Figure 20).

The results presented in Figure 20 demonstrate that the early-August peak in all eddy characteristics, as well as SC EKE, remains even when averaged across all years. It is worth noting, however, that these years only seem to affect maximums of these properties, less so the average values (Figures 20e–20h). This indicates that it is the largest and most energetic eddies that are being altered and that these eddies are in turn influencing the EKE of the SC as a whole. Given the consistent spikes and implications on major eddies, we proceed to examine the differences in the dynamics of the SC region between each type of year to determine possible causes.

We begin with a look at the average WSC of the region over time (Figure 21) as well as the covariance between the WSC and ADT (Figure 22) as previously seen in Figures 11 and 12. Figure 21 is different than Figure 12 in that the second and third columns are the differences between full years and half years and the differences between full and local years, respectively. This is to visualize the changes from 1 year type to another.

Here, we can view the onset of the summer monsoon and the Findlater Jet between May and June (Figures 21b , 21c, 21h, 21i, 21n, and 21o) and the subsequent swelling of the GW along the southern edge of the jet through the heavily negative covariance during the entire summer monsoon (Figures 22c–22f, 22i–22l, and 22o–22r). The most striking difference between the year modes is the region of much more negative WSC on the northern flank of the GW. There is also a more positive WSC on the eastern flank in July and August of both the half years (Figures 21j and 21k) and full years (Figures 21p and 21q). This more positive WSC may help induce the slightly greater peaks in the half and local years' SC EKE as compared to the full years in Figures 19 and 20. Furthermore, we observe a positive WSC and covariance on the eastern flank of the GW in local years in August (Figure 22q).

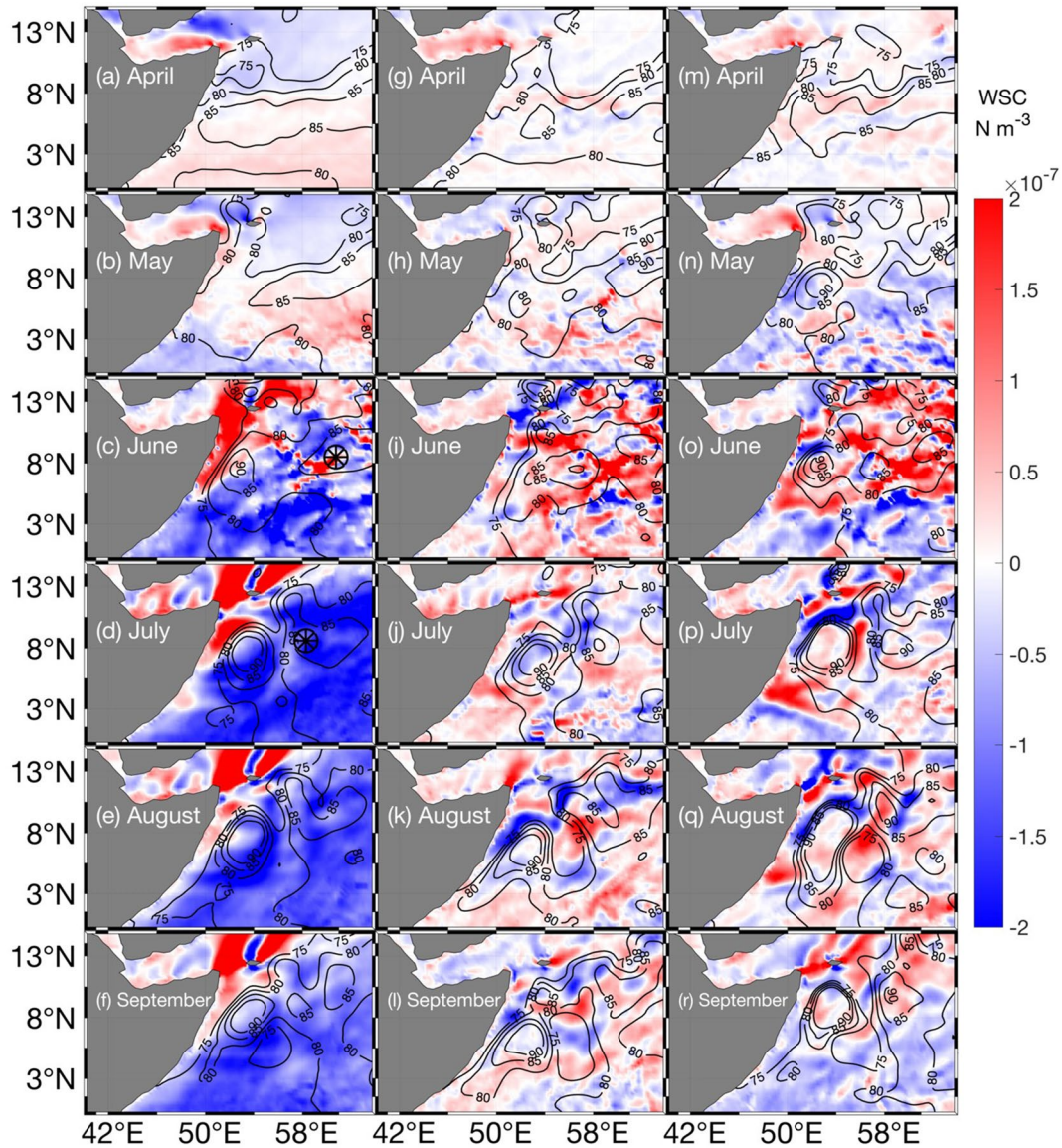

Figure 21. Wind stress curl (WSC) (N m^{-3}) differences between full, half, and local years for the first week in each month between April and September averaged across 1993–2019 in the Somali Current (SC) region. Contours depict absolute dynamic topography (ADT) (cm). Black pinwheels mark the average locations of the tracked Lakshadweep High (LH). (a–f) Average for full years. (g–i) Average for full years minus the average for half years. (m–r) Average for full years minus the average for local years.

This indicates an enhanced development of the cyclone that often orbits the GW from northwest to southeast (Beal & Donohue, 2013). As noted in Section 3.3, the variability of eddy killing within monsoons in the AS has not been studied. However, recent measurements of the radius of the GW indicate an average radius above 300 km (Melzer et al., 2019). Therefore, the GW and its cyclone, which reaches a similar size, are above the most recent estimates for the global eddy killing scale of 260 km (Rai et al., 2021). Together with Figure 22, this allows us to reasonably conclude the GW's growth and the growth of its orbiting cyclone are primarily due to the WSC over the region. The same conclusion applies to the LH as it typically grows in the SC in July (Figure 22d).

In order to assess the growth of the GW and its cyclone independently, we separate the amplitude, radius, and EKE of the SC between AEs and cyclonic eddies (CEs) (Figure 23).

We find that the properties of the measured eddies match with previously established analyses in the region in all years (Trott, Subrahmanyam, & Murty, 2017; Trott, Subrahmanyam, Chaigneau, Delcroix, 2018). While the

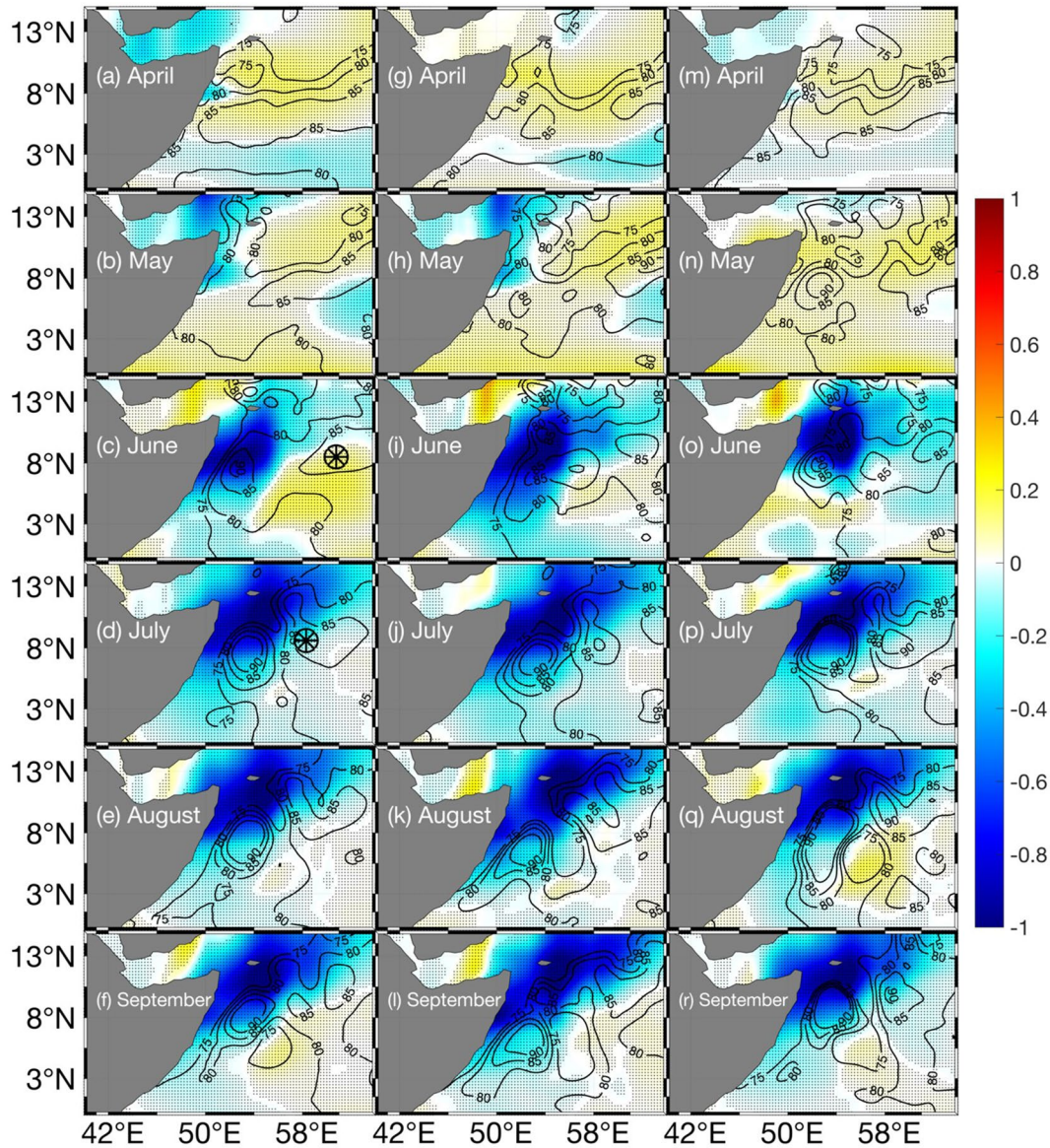

Figure 22. The same spatiotemporal area as Figure 22, but plotting the normalized covariance (color) and significant correlations (shading) between the Wind stress curl (WSC) and the absolute dynamic topography (ADT) (as in Figure 12.) Contours are ADT, the same as Figure 21.

previous mid-August spikes are evident in all profiles, of specific note is the magnitude of the scales involved. The spikes in CE amplitude and EKE (Figures 23b and 23f) are twice those of their respective AE profiles (Figures 23a and 23e). Given that the circulation of the GW is always anticyclonic, this indicates that these spikes are present partially due to changes in the GW but more so due to the growth of a significantly larger cyclonic circulation. As seen in the average ADT of the SC region in local years in the first week of August (Figure 22q), the cyclone that orbits around the GW is the most likely culprit for this spike, as no other CE approaches its size in the region.

We test this hypothesis by inspecting the ADT of the region per year during this spiking time period (Figure 24). We observe that the average case of the late July to early August cyclone is relatively indistinct in full and half years (Figures 24a–24e and 24f–24j) but is particularly well pronounced during local years (Figures 24k–24o). The ADT profile moving into August shows an elongated GW and a large, circular orbiting cyclone (Figure 24i), which corresponds to the time period during which the EKE of the region is increasing. This culminates in the

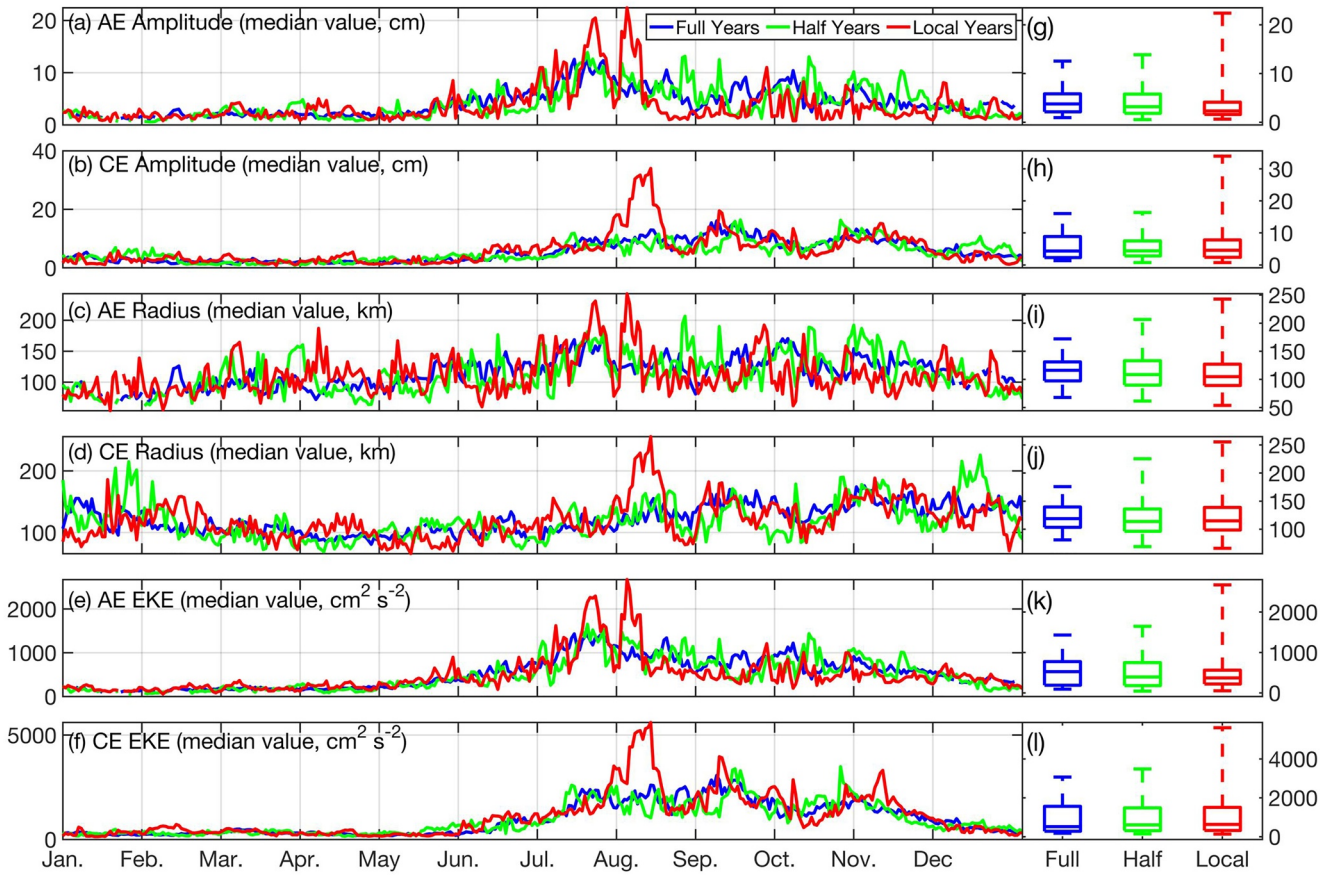

Figure 23. Yearlong characteristics of eddies in the Somali Current averaged between 1993 and 2019 (as in Figure 20) but separated between anticyclonic eddies (AEs) and cyclonic eddies (CEs). Blue lines depict full years, green lines depict half years, and red lines depict local years. (a) Median AE amplitude (cm), (b) same as (a) but for CEs. (c) Median AE radius (km). (d) same as (c) but for CEs. (e) Median average AE EKE (cm^2 s^{-2}). (f) same as (e) but for CEs. Note that there is a difference in the *y*-axis scales between AEs and CEs.

early August spike (Figure 24m) where the orbiting cyclone has moved to the south of the GW and is at its maximum extent. The decrease in the region's EKE continues as the cyclone diminishes into mid-August (Figure 24n) before becoming indistinct in late August (Figure 24o). This larger GW-related cyclone in the local years is also partially seen in Beal and Donohue (2013)'s Figure 10.

Besides the WSC facilitating the growth of the cyclone, we hypothesize that the arrival of the stronger Rossby wave carrying LH in full and half years (Figure 14) may be inhibiting its development. To explore this possibility, we again look at the 3D profile of the 2006 LH, this time as it arrives in the SC region, 1,845 km westward and only 10 km southward of its original position in Figure 8 (Figure 25).

We see in the ADT profile the previous GW orbiting cyclone to the southwest and the next orbiting cyclone to the northwest (Figure 25a), with a GW that is at this point smaller in amplitude and radius than the LH itself. The geostrophic currents still show a strong circulation around the LH, but with contours that stretch around the GW system. However, unlike in the previous profiles where currents flowed between eddies (Figures 17 and 18), this LH is more distinct in terms of its SSS and SST as compared to the GW (Figures 25b and 25c). We observe a warm core to the LH as compared to the cold frontal zone of the GW, a sign of the AS water that now forms the entirety of the LH clashing with some of the more equatorial waters of the GW and SC as a whole (Figures 25c and 25g). In this stage of its life, the LH's BoB water lens of fresher water has been entirely obliterated in the subsurface profile (Figures 25b and 25f), and the spiciness provides evidence to suggest that the water masses in the region are now more heavily temperature controlled than salinity controlled (Figure 25d). These properties combine to form a relatively deep mixed layer (Figure 25d). Lastly, the vertical velocity profile is similarly distinct, with a positive column to the east of the LH and a negative layer beneath 100 m to the west (Figure 25h).

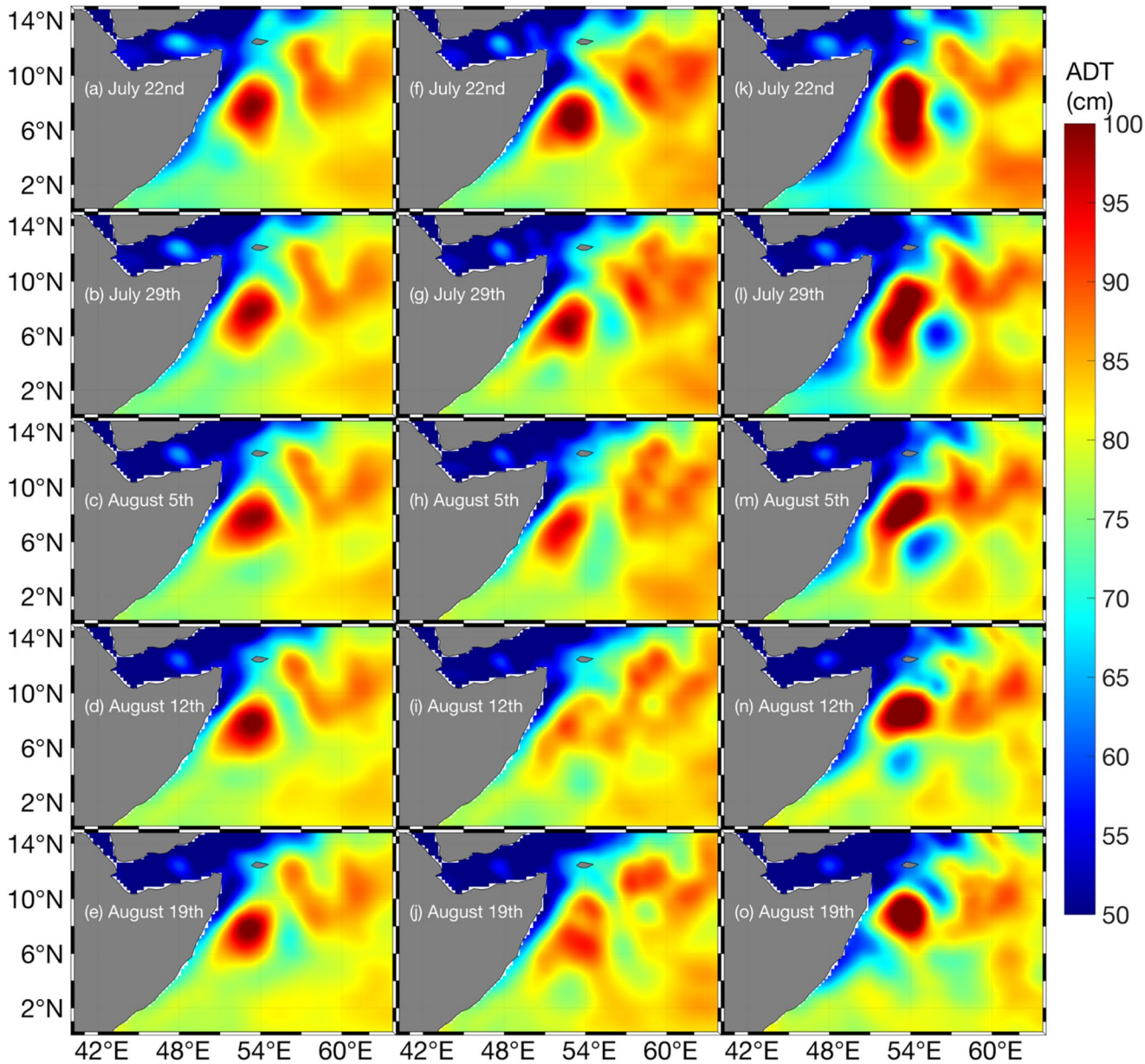

Figure 24. The average absolute dynamic topography (ADT) (cm) of the SC region between 1993 and 2019 per type of Lakshadweep High (LH) propagation year. Full years: (a) July 22nd, (b) July 29th, (c) August 5th, (d) August 12th, and (e) August 19th (f–j) same as (a–e) but for half years (k–o) same as (a–e) but for local years.

The future of this LH is, as visualized in its trajectory (Figure 4a), to shift westward as the GW shifts to the northeast, reaching a maximum radius of 375 km. As it moves into position and grows, the GW cyclone can no longer form, and so it prevents the spike seen in the SC EKE (Figure 21d). The 2006 full LH finally loses coherence on October 26th, achieving a total lifespan of 319 days.

4. Conclusions

The variability of the eddy field in the AS plays a critical role in the modulation of air-sea fluxes and the transport of water masses across the basin. However, little attention has been given in recent years to the LH and none of the current high-resolution altimetric data sets or reanalysis products have been used to analyze its interannual variability and the possible consequences therein. In this study, we have used the closed-contour eddy tracking algorithm previously used by Trott, Subrahmanyam, Chaigneau and Delcroix (2018) in the AS to track the LH

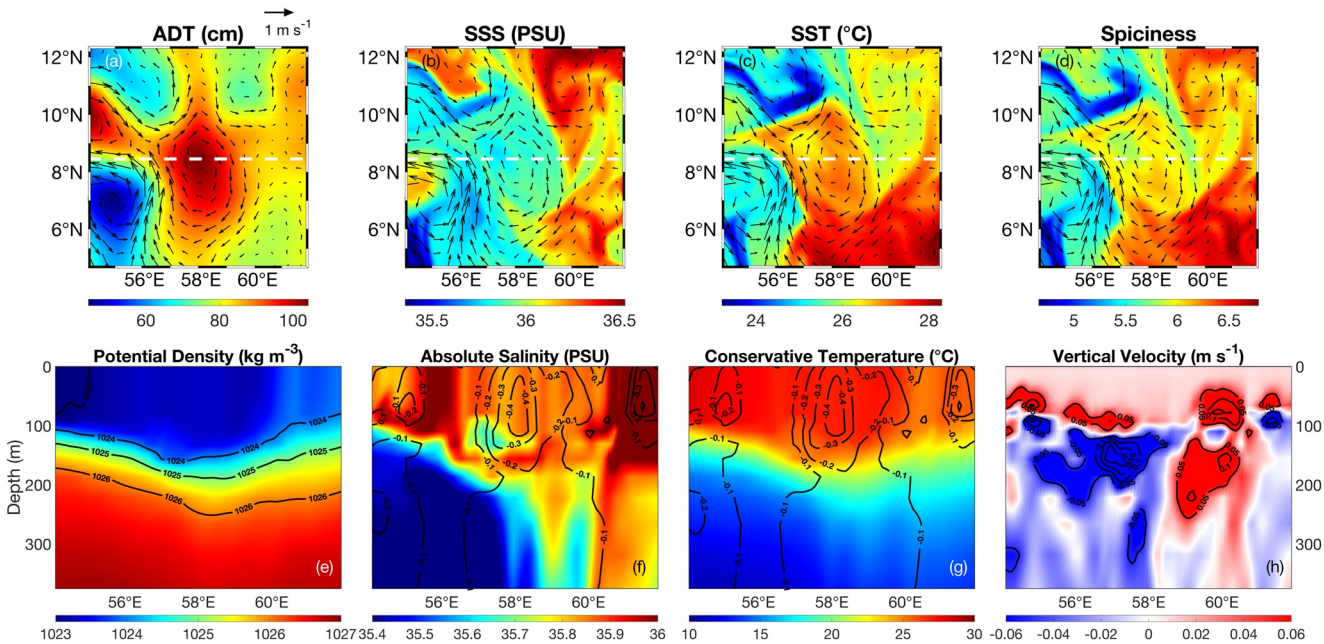

Figure 25. Same as Figure 8 but for the location marked in Figure 3c for the full example year (21 July 2006).

through the course of the year. We examined the different processes that contribute to the phases of the LH's life cycle and provided observational evidence that supports past hypotheses regarding the LH, such as those by Shankar and Shetye (1997) and Bruce et al. (1998), while arriving at new findings regarding the LH's impact on the GW and the SC region.

We began with a full-life trajectory analysis of the LH, categorizing it into three distinct types of propagation (full, half, and local) based on its eventual location of decoherence. We correlated drifter trajectories with that of LH, determining the error of the altimetric geostrophic currents. The dynamics of the origin of the LH are then considered, with a conclusion that the second annual downwelling CKW is the major phenomenon responsible, though the forcing of this wave by wind stress in the STIP region is another likely factor. We identify that different strengths of CKW correlate with the type of propagation of LH. At this stage and each step thereafter, we provide 3D profiles of the LH, allowing for a more in-depth analysis of the water masses involved in the LH over its life. We continued with an inspection of the WSC over the LH demonstrating that it is both a complex factor that may detract from the initial growth and maintenance of the LH and a differentiator that separates the modes of LH propagation. After the LH's growth, we further inspect the primary westward propagation mechanism of the LH, the Rossby wave along 8°N, and find that its speed and the speed of the LH both agree with each other and the theoretical speeds of the region. It is at this point that we note that in full years, fresher BoB water is pulled by the LH past 70°N into the center of the AS. With the coherent propagation of LH thus established, we study its effects on the SC, and its eventual destination. We hypothesize that the WSC of the region fuels a larger GW in most local years, while the arrival of the LH in full years may inhibit the growth of a larger cyclone in the beginning of August. This causes a steeper peak to occur in the outlier local years, and to a lesser extent in the half years.

Our new evaluation of the LH indicates that it is a more long-lived and far-reaching phenomenon than previously considered. We also demonstrate that there are a myriad of ill-studied factors and limitations to this study that must be addressed in order to complete a total understanding of the LH phenomenon. We acknowledge that the resolution of current altimetry products is insufficient to capture the totality of the eddy field, and may be falsely aggregating smaller eddies into larger formations (Amores et al., 2018). Likewise, there remain questions regarding the linkage between ENSO and IOD, as well as their exact effects on the winter monsoon and CKW propagation (e.g., McKenna et al., 2020). With these factors in mind, we formulate a few lingering questions beyond the scope of our study. These include the effect of eddy killing throughout the AS, the effects of submesoscale energy transfer via eddy splitting/merging events in the AS, and the variability of these factors by monsoon. When these questions and those following them are answered, whether by further investigation using existing

techniques (e.g., Rai et al., 2021), new algorithms (e.g., Tian et al., 2021), and/or improved observations, such as from the upcoming National Aeronautics and Space Administration (NASA) SWOT mission, we will understand the LH phenomenon.

Conflict of Interest

The authors declare no conflicts of interest relevant to this study.

Data Availability Statement

ADT, SLA, and geostrophic current data from the Copernicus Marine Environmental Service (CMEMS) can be found at https://resources.marine.copernicus.eu/?option=com_csw&view=details&product_id=SEALEVEL_GLO_PHY_L4_REP_OBSERVATIONS_008_047. The NOAA Blended Sea Winds data set is available at https://www.ncei.noaa.gov/products/blended-sea-winds and the NOAA Global Drifter Program data are available at http://osmc.noaa.gov/erddap/tabledap/gdp_interpolated_drifter.html. Finally, the GLORYS12v1 reanalysis data set is maintained by CMEMS at https://resources.marine.copernicus.eu/?option=com_csw&view=details&product_id=GLOBAL_REANALYSIS_PHY_001_030. Data for Table 1 were adapted from Roman-Stork et al. (2020) and expanded upon from the same sources as that study: Monsoon phase (strong, weak, or normal) data were pulled from the Indian Institute of Tropical Meteorology (https://www.tropmet.res.in/~kolli/MOL/Monsoon/Historical/air.html); El Niño Southern Oscillation phases were taken from the NOAA and National Center for Environment Prediction Oceanic Niño Index; Indian Ocean Dipole annual phases were taken from the Australian Bureau of Meteorology (http://www.bom.gov.au/climate/iod/).

Acknowledgments
This work is supported by ONR Award #N00014-20-1-2742 awarded to BS. PE is funded by the U.S. Department of Defense Science, Mathematics, and Research for Transformation (SMART) Scholarship and the University of South Carolina Presidential Fellowship. This has NRL contribution number JA-7320-22-5347. Approved for public release and distribution is unlimited. The authors thank the reviewers and editor for their insightful comments that contributed significantly to the improvement of the paper.

References

Akuetevi, C. Q. C., Barnier, B., Verron, J., Molines, J.-M., & Lecointre, A. (2016). Interactions between the Somali current eddies during the summer monsoon: Insights from a numerical study. *Ocean Science*, *12*(1), 185–205. https://doi.org/10.5194/os-12-185-2016

Amores, A., Jordà, G., Arsouze, T., & Sommer, J. L. (2018). Up to what extent can we characterize ocean eddies using present-day gridded altimetric products? *Journal of Geophysical Research: Oceans*, *123*(10), 7220–7236. https://doi.org/10.1029/2018JC014140

Beal, L. M., & Donohue, K. A. (2013). The Great Whirl: Observations of its seasonal development and interannual variability. *Journal of Geophysical Research: Oceans*, *118*(1), 1–13. https://doi.org/10.1029/2012JC008198

Beal, L. M., Hormann, V., Lumpkin, R., & Foltz, G. R. (2013). The response of the surface circulation of the Arabian Sea to monsoonal forcing. *Journal of Physical Oceanography*, *43*(9), 2008–2022. https://doi.org/10.1175/JPO-D-13-033.1

Brandt, P., Stramma, L., Schott, F., Fischer, J., Dengler, M., & Quadfasel, D. (2002). Annual Rossby waves in the Arabian Sea from TOPEX/POSEIDON altimeter and in situ data. *Deep Sea Research Part II: Topical Studies in Oceanography*, *49*(7), 1197–1210. https://doi.org/10.1016/S0967-0645(01)00166-7

Bruce, J. G. (1983). The wind field in the western Indian ocean and the related ocean circulation. *Monthly Weather Review*, *111*(7), 1442–1452. https://doi.org/10.1175/1520-0493(1983)111<1442:twfitw>2.0.co;2

Bruce, J. G., Johnson, D. R., & Kindle, J. C. (1994). Evidence for eddy formation in the eastern Arabian Sea during the northeast monsoon. *Journal of Geophysical Research: Oceans*, *99*(C4), 7651–7664. https://doi.org/10.1029/94JC00035

Bruce, J. G., Kindle, J. C., Kantha, L. H., Kerling, J. L., & Bailey, J. F. (1998). Recent observations and modeling in the Arabian Sea Laccadive high region. *Journal of Geophysical Research:*, *103*(C4), 7593–7600. https://doi.org/10.1029/97JC03219

Calil, P. H. R., Richards, K. J., Jia, Y., & Bidigare, R. R. (2008). Eddy activity in the lee of the Hawaiian Islands. *Deep Sea Research Part II: Topical Studies in Oceanography*, *55*(10), 1179–1194. https://doi.org/10.1016/j.dsr2.2008.01.008

Chaigneau, A., Gizolme, A., & Grados, C. (2008). Mesoscale eddies off Peru in altimeter records: Identification algorithms and eddy spatio-temporal patterns. *Progress in Oceanography*, *79*(2), 106–119. https://doi.org/10.1016/j.pocean.2008.10.013

Challenor, P. G., Cipollini, P., & Cromwell, D. (2001). Use of the 3D Radon transform to examine the properties of oceanic Rossby waves. *Journal of Atmospheric and Oceanic Technology*, *18*(9), 1558–1566. https://doi.org/10.1175/1520-0426(2001)018<1558:uotrtt>2.0.co;2

Chelton, D. B., Schlax, M. G., & Samelson, R. M. (2011). Global observations of nonlinear mesoscale eddies. *Progress in Oceanography*, *91*(2), 167–216. https://doi.org/10.1016/j.pocean.2011.01.002

Cui, W., Wang, W., Zhang, J., & Yang, J. (2019). Multicore structures and the splitting and merging of eddies in global oceans from satellite altimeter data. *Ocean Science*, *15*(2), 413–430. https://doi.org/10.5194/os-15-413-2019

Dai, A., Qian, T., Trenberth, K. E., & Milliman, J. D. (2009). Changes in continental freshwater discharge from 1948 to 2004. *Journal of Climate*, *22*(10), 2773–2792. https://doi.org/10.1175/2008JCLI2592.1

Deans, S. R. (2007). *The Radon transform and some of its applications*. Courier Corporation.

de Marez, C., Carton, X., L'Hégaret, P., Meunier, T., Stegner, A., Le Vu, B., & Morvan, M. (2020). Oceanic vortex mergers are not isolated but influenced by the β -effect and surrounding eddies. *Scientific Reports*, *10*(1),2897. https://doi.org/10.1038/s41598-020-59800-y

de Marez, C., L'Hégaret, P., Morvan, M., & Carton, X. (2019). On the 3D structure of eddies in the Arabian Sea. *Deep Sea Research Part I: Oceanographic Research Papers*, *150*, 103057. https://doi.org/10.1016/j.dsr.2019.06.003

Ducet, N., Le Traon, P. Y., & Reverdin, G. (2000). Global high-resolution mapping of ocean circulation from TOPEX/Poseidon and ERS-1 and -2. *Journal of Geophysical Research: Oceans*, *105*(C8), 19477–19498. https://doi.org/10.1029/2000JC900063

Durand, F., Shankar, D., Birol, F., & Shenoi, S. S. C. (2009). Spatiotemporal structure of the east India coastal current from satellite altimetry. *Journal of Geophysical Research: Oceans*, *114*(C2). https://doi.org/10.1029/2008JC004807

Echols, R., & Riser, S. C. (2020). Spice and barrier layers: An Arabian Sea case study. *Journal of Physical Oceanography*, *50*(3), 695–714. https://doi.org/10.1175/JPO-D-19-0215.1

Findlater, J. (1969). A major low-level air current near the Indian Ocean during the northern summer. *Quarterly Journal of the Royal Meteorological Society*, *95*(404), 362–380. https://doi.org/10.1002/qj.49709540409

Fischer, A. S., Weller, R. A., Rudnick, D. L., Eriksen, C. C., Lee, C. M., Brink, K. H., et al. (2002). Mesoscale eddies, coastal upwelling, and the upper-ocean heat budget in the Arabian Sea. *Deep Sea Research Part II: Topical Studies in Oceanography*, *49*(12), 2231–2264. https://doi.org/10.1016/S0967-0645(02)00036-X

Franz, K., Roscher, R., Milioto, A., Wenzel, S., & Kusche, J. (2018). *Ocean eddy identification and tracking using neural networks*. ArXiv:1803.07436 [Cs]. Retrieved from http://arxiv.org/abs/1803.07436

Greaser, S. R., Subrahmanyam, B., Trott, C. B., & Roman-Stork, H. L. (2020). Interactions between mesoscale eddies and synoptic oscillations in the Bay of Bengal during the strong monsoon of 2019. *Journal of Geophysical Research: Oceans*, *125*(10), e2020JC016772. https://doi.org/10.1029/2020JC016772

Heffner, D. M., Subrahmanyam, B., & Shriver, J. F. (2008). Indian Ocean Rossby waves detected in HYCOM sea surface salinity. *Geophysicaal Research Letters*, *35*, L03605. https://doi.org/10.1029/2007GL032760

Izumo, T., Montégut, C. B., Luo, J.-J., Behera, S. K., Masson, S., & Yamagata, T. (2008). The role of the Western Arabian Sea upwelling in Indian monsoon rainfall variability. *Journal of Climate*, *21*(21), 5603–5623. https://doi.org/10.1175/2008JCLI2158.1

Izumo, T., Vialard, J., Lengaigne, M., de Boyer Montegut, C., Behera, S. K., Luo, J.-J., et al. (2010). Influence of the state of the Indian Ocean Dipole on the following year's El Niño. *Nature Geoscience*, *3*(3), 168–172. https://doi.org/10.1038/ngeo760

Jensen, T. G. (2007). Wind-driven response of the northern Indian Ocean to climate extremes. *Journal of Climate*, *20*(13), 2978–2993. https://doi.org/10.1175/JCLI4150.1

Kurian, J., & Vinayachandran, P. N. (2007). Mechanisms of formation of the Arabian Sea mini warm pool in a high-resolution ocean general circulation model. *Journal of Geophysical Research*, *112*(C5). https://doi.org/10.1029/2006JC003631

Lellouche, J.-M., Le Galloudec, O., Greiner, E., Garric, G., Regnier, C., Drevillon, M., et al. (2018). *The Copernicus marine environment monitoring Service global ocean 1/12° physical reanalysis GLORYS12V1: Description and quality assessment, 19806*. Presented at the EGU General Assembly Conference Abstracts.

Le Traon, P. Y., Nadal, F., & Ducet, N. (1998). An improved mapping method of multisatellite altimeter data. *Journal of Atmospheric and Oceanic Technology*, *15*, 522–534. https://doi.org/10.1175/1520-0426(1998)015<0522:aimmom>2.0.co;2

Le Vu, B., Stegner, A., & Arsouze, T. (2018). Angular momentum eddy detection and tracking algorithm (AMEDA) and its application to coastal eddy formation. *Journal of Atmospheric and Oceanic Technology*, *35*(4), 739–762. https://doi.org/10.1175/JTECH-D-17-0010.1

L'Hégaret, P., Carton, X., Louazel, S., & Boutin, G. (2016). Mesoscale eddies and submesoscale structures of Persian Gulf Water off the Omani coast in spring 2011. *Ocean Science*, *12*(3), 687–701. https://doi.org/10.5194/os-12-687-2016

Liu, B., Wu, G., & Ren, R. (2015). Influences of ENSO on the vertical coupling of atmospheric circulation during the onset of South Asian summer monsoon. *Climate Dynamics*, *45*(7), 1859–1875. https://doi.org/10.1007/s00382-014-2439-3

Ma, X., Jing, Z., Chang, P., Liu, X., Montuoro, R., Small, R. J., et al. (2016). Western boundary currents regulated by interaction between ocean eddies and the atmosphere. *Nature*, *535*(7613), 533–537. https://doi.org/10.1038/nature18640

McDougall, T. J., & Krzysik, O. A. (2015). Spiciness. *Journal of Marine Research*, *73*(5), 141–152. https://doi.org/10.1357/002224015816665589

McKenna, S., Santoso, A., Gupta, A. S., Taschetto, A. S., & Cai, W. (2020). Indian Ocean Dipole in CMIP5 and CMIP6: Characteristics, biases, and links to ENSO. *Scientific Reports*, *10*(1), 11500. https://doi.org/10.1038/s41598-020-68268-9

Melzer, B. A., Jensen, T. G., & Rydbeck, A. V. (2019). Evolution of the Great Whirl using an altimetry-based eddy tracking algorithm. *Geophysical Research Letters*, *46*(8), 4378–4385. https://doi.org/10.1029/2018GL081781

Murtugudde, R., & Busalacchi, A. J. (1999). Interannual variability of the dynamics and thermodynamics of the Tropical Indian ocean. *Journal of Climate*, *12*(8), 2300–2326. https://doi.org/10.1175/1520-0442(1999)012<2300:ivotda>2.0.co;2

Pegliasco, C., Chaigneau, A., & Morrow, R. (2015). Main eddy vertical structures observed in the four major Eastern Boundary Upwelling Systems. *Journal of Geophysical Research: Oceans*, *120*(9), 6008–6033. https://doi.org/10.1002/2015JC010950

Polito, P. S., & Sato, O. T. (2015). Do eddies ride on Rossby waves? *Journal of Geophysical Research: Oceans*, *120*(8), 5417–5435. https://doi.org/10.1002/2015JC010737

Prasad, T. G., & Ikeda, M. (2001). Spring evolution of Arabian Sea high in the Indian ocean. *Journal of Geophysical Research*, *106*(C12), 31085–31098. https://doi.org/10.1029/2000JC000314

Rai, S., Hecht, M., Maltrud, M., & Aluie, H. (2021). Scale of oceanic eddy killing by wind from global satellite observations. *Science Advances*, *7*(28), eabf4920. https://doi.org/10.1126/sciadv.abf4920

Rao, A. D., Joshi, M., & Ravichandran, M. (2008). Oceanic upwelling and downwelling processes in waters off the west coast of India. *Ocean Dynamics*, *58*(3–4), 213–226. https://doi.org/10.1007/s10236-008-0147-4

Rao, R. R., Girish Kumar, M. S., Ravichandran, M., Rao, A. R., Gopalakrishna, V. V., & Thadathil, P. (2010). Interannual variability of Kelvin wave propagation in the wave guides of the equatorial Indian Ocean, the coastal Bay of Bengal and the southeastern Arabian Sea during 1993–2006. *Deep Sea Research Part I: Oceanographic Research Papers*, *57*(1), 1–13. https://doi.org/10.1016/j.dsr.2009.10.008

Roman-Stork, H. L., Subrahmanyam, B., & Murty, V. S. N. (2020). The role of salinity in the southeastern Arabian Sea in determining monsoon onset and strength. *Journal of Geophysical Research: Oceans*, *125*(1), e2019JC015592. https://doi.org/10.1029/2019JC015592

Schott, F., Reppin, J., Fischer, J., & Quadfasel, D. (1994). Currents and transports of the monsoon current south of Sri Lanka. *Journal of Geophysical Research*, *99*(C12), 25127–25141. https://doi.org/10.1029/94JC02216

Schott, F. A., & McCreary, J. P. (2001). The monsoon circulation of the Indian Ocean. *Progress in Oceanography*, *51*(1), 1–123. https://doi.org/10.1016/S0079-6611(01)00083-0

Seo, H. (2017). Distinct influence of air–sea interactions mediated by mesoscale sea surface temperature and surface current in the Arabian Sea. *Journal of Climate*, *30*(20), 8061–8080. https://doi.org/10.1175/JCLI-D-16-0834.1

Shankar, D., & Shetye, S. R. (1997). On the dynamics of the Lakshadweep high and low in the southeastern Arabian Sea. *Journal of Geophysical Research*, *102*(C6), 12551–12562. https://doi.org/10.1029/97JC00465

Shenoi, S. S. C., Shankar, D., Michael, G. S., Kurian, J., Varma, K. K., Kumar, M. R. R., et al. (2005). Hydrography and water masses in the southeastern Arabian Sea during March–June 2003. *Journal of Earth System Science*, *114*(5), 475–491. https://doi.org/10.1007/BF02702024

Shukla, J. (1975). Effect of Arabian Sea-surface temperature anomaly on Indian summer monsoon: A numerical experiment with the GFDL model. *Journal of the Atmospheric Sciences*, *32*(3), 503–511. https://doi.org/10.1175/1520-0469(1975)032<0503:eoasst>2.0.co;2

Subrahmanyam, B., Heffner, D. M., Cromwell, D., & Shriver, J. F. (2009). Detection of Rossby waves in multi-parameters in multi-mission satellite observations and HYCOM simulations in the Indian Ocean. *Remote Sensing of Environment*, *113*(6), 1293–1303. https://doi.org/10.1016/j.rse.2009.02.017

Subrahmanyam, B., Robinson, I. S., Blundell, J. R., & Challenor, P. G. (2001). Indian Ocean Rossby waves observed in TOPEX/POSEIDON altimeter data and in model simulations. *International Journal of Remote Sensing*, *22*(1), 141–167. https://doi.org/10.1080/014311601750038893

Subrahmanyam, B., Roman-Stork, H. L., & Murty, V. S. N. (2020). Response of the Bay of Bengal to 3-7-day synoptic oscillations during the southwest monsoon of 2019. *Journal of Geophysical Research: Oceans*, *125*(6), e2020JC016200. https://doi.org/10.1029/2020JC016200

Suresh, I., Vialard, J., Izumo, T., Lengaigne, M., Han, W., McCreary, J., & Muraleedharan, P. M. (2016). Dominant role of winds near Sri Lanka in driving seasonal sea level variations along the west coast of India. *Geophysical Research Letters*, *43*(13), 7028–7035. https://doi.org/10.1002/2016GL069976

Tian, F., Li, Z., Yuan, Z., & Chen, G. (2021). EddyGraph: The tracking of mesoscale eddy splitting and merging events in the northwest Pacific ocean. *Remote Sensing*, *13*(17), 3435. https://doi.org/10.3390/rs13173435

Tozuka, T., Nagura, M., & Yamagata, T. (2014). Influence of the reflected Rossby waves on the Western Arabian Sea upwelling region. *Journal of Physical Oceanography*, *44*(5), 1424–1438. https://doi.org/10.1175/JPO-D-13-0127.1

Trott, C. B., Subrahmanyam, B., Chaigneau, A., & Delcroix, T. (2018). Eddy tracking in the northwestern Indian ocean during southwest monsoon regimes. *Geophysical Research Letters*, *45*(13), 6594–6603. https://doi.org/10.1029/2018GL078381

Trott, C. B., Subrahmanyam, B., Chaigneau, A., & Roman-Stork, H. L. (2019). Eddy-induced temperature and salinity variability in the Arabian Sea. *Geophysical Research Letters*, *46*(5), 2734–2742. https://doi.org/10.1029/2018GL081605

Trott, C. B., Subrahmanyam, B., & Murty, V. S. N. (2017). Variability of the Somali Current and eddies during the southwest monsoon regimes. *Dynamics of Atmospheres and Oceans*, *79*, 43–55. https://doi.org/10.1016/j.dynatmoce.2017.07.002

Vecchi, G. A., Xie, S.-P., & Fischer, A. S. (2004). Ocean–Atmosphere covariability in the Western Arabian Sea. *Journal of Climate*, *17*(6), 1213–1224. https://doi.org/10.1175/1520-0442(2004)017<1213:ocitwa>2.0.co;2

Verezemskaya, P., Barnier, B., Gulev, S. K., Gladyshev, S., Molines, J.-M., Gladyshev, V., et al. (2021). Assessing eddying (1/12°) ocean reanalysis GLORYS12 using the 14-yr instrumental record from 59.5°N section in the Atlantic. *Journal of Geophysical Research: Oceans*, *126*(6), e2020JC016317. https://doi.org/10.1029/2020JC016317

Vic, C., Roullet, G., Carton, X., & Capet, X. (2014). Mesoscale dynamics in the Arabian Sea and a focus on the Great Whirl life cycle: A numerical investigation using ROMS. *Journal of Geophysical Research: Oceans*, *119*(9), 6422–6443. https://doi.org/10.1002/2014JC009857

Wang, S., Zhu, W., Ma, J., Ji, J., Yang, J., & Dong, C. (2019). Variability of the Great Whirl and its impacts on atmospheric processes. *Remote Sensing*, *11*(3), 322. https://doi.org/10.3390/rs11030322

Williams, S., Petersen, M., Bremer, P.-T., Hecht, M., Pascucci, V., Ahrens, J., et al. (2011). Adaptive extraction and quantification of geophysical vortices. *IEEE Transactions on Visualization and Computer Graphics*, *17*(12), 2088–2095. https://doi.org/10.1109/TVCG.2011.162

Yuan, Y., Yang, H., Zhou, W., & Li, C. (2008). Influences of the Indian Ocean Dipole on the Asian summer monsoon in the following year. *International Journal of Climatology*, *28*, 1849–1859. https://doi.org/10.1002/joc.1678

Zachariah, J., Babu, C. A., & Varikoden, H. (2019). Dynamics of westward propagation and intensification of Lakshadweep low in the southern Arabian Sea. *Ocean Dynamics*, *69*(5), 519–528. https://doi.org/10.1007/s10236-019-01263-5

Zhan, P., Guo, D., & Hoteit, I. (2020). Eddy-induced transport and kinetic energy budget in the Arabian Sea. *Geophysical Research Letters*, *47*(23), e2020GL090490. https://doi.org/10.1029/2020GL090490

Zhang, Z., Wang, W., & Qiu, B. (2014). Oceanic mass transport by mesoscale eddies. *Science*, *345*(6194), 322–324. https://doi.org/10.1126/science.1252418

Zhang, Z., Zhao, W., Qiu, B., & Tian, J. (2017). Anticyclonic eddy sheddings from Kuroshio Loop and the accompanying cyclonic eddy in the Northeastern south China Sea. *Journal of Physical Oceanography*, *47*(6), 1243–1259. https://doi.org/10.1175/JPO-D-16-0185.1